ELSEVIER

Contents lists available at ScienceDirect

Atmospheric Research

journal homepage: www.elsevier.com/locate/atmosres





Modeling initial breakdown pulses of intracloud lightning flashes

Nilmini Karunarathne, Thomas C. Marshall, Sumedhe Karunarathne, Maribeth Stolzenburg

Department of Physics and Astronomy, University of Mississippi, MS, USA

ARTICLE INFO

Keywords:
Lightning
Intracloud lightning
Initial breakdown pulses
IBPs
Preliminary breakdown pulses
Matrix inversion

ABSTRACT

In this study 29 initial breakdown pulses (IBPs) from four intracloud (IC) lightning flashes are modeled using data from five or more electric field change (*E*-change) sites. For each flash the first 5–9 located IBPs are investigated. For each IBP the modeling first extracts the IBP current waveform from the *E*-change data by matrix inversion and then determines the best channel length and current velocity to match the IBP data. Derived IBP quantities of total charge, charge moment, peak current, peak radiated power, and total energy are calculated. Resulting IBP vertical lengths varied from 27 m to 1300 m; most values were 100–500 m. Current velocities ranged over $4.0-20.0 \times 10^7$ m/s, with most values $10-16.5 \times 10^7$ m/s. Two of these IC flashes had two "extraordinary" IBPs each with very large *E*-change amplitude and multiple subpulses; these four extraordinary IBPs had longer current rise times than fall times and charge moments of -3.45 to -20.06C km. Subpulses of classic IBPs were coincident with, and likely caused by, smaller current pulses superimposed on the main IBP current. Overall, most of the 29 IC IBPs had peak current amplitudes <120 kA and total (negative) charge <2C, while the four extraordinary IBPs all have the characteristics of Energetic In-cloud Pulses (EIPs), which are thought to be the radio signals of events producing terrestrial gamma-ray flashes (TGFs). The extraordinary IBPs may have caused double-pulse TGFs and overlapping TGFs.

1. Introduction

The intracloud (IC) lightning discharge, occurring within cloud and not connecting to ground, was first studied with electric field measurements by Smith (1957). Many studies since then have focused on IC flashes because of their unique characteristics (e.g., Kitagawa and Brook, 1960; Ogawa and Brook, 1964; Bils et al., 1988; Villanueva et al., 1994; Shao and Krehbiel, 1996). Generally, normal IC flashes initiate just above a negative charge region in the thunderstorm and extend upward into a positive charge region. (e.g., Shao and Krehbiel, 1996; Coleman et al., 2003). Immediately after initiation, the initial breakdown (IB) stage occurs, with duration typically <20 ms in IC flashes but sometimes lasting longer (Villanueva et al., 1994).

The IB stage is characterized by the relatively large amplitude electromagnetic pulses that occur during it (e.g., Villanueva et al., 1994). Many studies have used electric field change (*E*-change) data to identify initial breakdown pulses (IBPs) (e.g., Clarence and Malan, 1957; Kitagawa and Brook, 1960; Weidman and Krider, 1979; Beasley et al., 1982; Villanueva et al., 1994; Marshall et al., 2013; Karunarathne et al., 2014;

Stolzenburg et al., 2016; Shi et al., 2019). Marshall et al. (2013) classified IBPs into "narrow" IBPs with durations <4 µs, "intermediate" IBPs with durations between 4 and 10 μ s, and "classic" IBPs with durations $\geq \! 10$ µs. It is commonly observed that classic IBPs usually have much larger pulse amplitudes than narrow or intermediate IBPs. Normally, the classic IBPs of IC flashes show a basic bipolar waveform in E-change data, similar to classic cloud-to-ground (CG) IBPs (e.g., Marshall et al., 2013; Stolzenburg et al., 2016). However, IC IBPs differ from CG IBPs in many ways (e.g., Smith et al., 2018). The major difference is the polarity of the pulses. Using the physics convention of electric field polarity, the initial half cycle of the IC IBP is positive, which is the opposite polarity of CG IBPs (e.g., Weidman and Krider, 1979). The second different factor is that most classic IBPs of IC flashes typically have more fast rising subpulses superimposed on the initial half cycle of the main bipolar pulse (Weidman and Krider, 1979; Marshall et al., 2013; Stolzenburg et al., 2016). Subpulses are also observed in classic CG IBPs, but classic CG IBPs generally have fewer and smaller subpulses. A third important character of IC IBPs is that terrestrial gamma ray flashes (TGFs) have been detected coincident with them (e.g., Cummer et al., 2015); this

^{*} Corresponding author.

E-mail address: marshall@phy.olemiss.edu (T.C. Marshall).

¹ Present address: FedEx Business Intelligence and Analytics Services, 3620 Hacks Cross Rd., Memphis, TN 38125, USA.

coincidence has not been observed with CG IBPs. Marshall et al. (2013) studied large IBPs in ten IC flashes using wideband *E*-change data, multiband magnetic field change data, and VHF lightning mapping data to identify IBPs that were TGF 'candidate' pulses (IBPs that were likely to have produced TGFs). Although several TGFs have coincident magnetic field change data (e.g., Cummer et al., 2014, 2015; Lyu et al., 2016), so far only one TGF has been found with coincident wideband *E*-change measurements: Marshall et al. (2017) showed that the TGF-coincident event was probably a large amplitude, classic IBP of an IC flash.

To date no study has attempted to find the behavior of the current during the IB stage of IC flashes, even though current is a potentially useful parameter to help understand the mechanism of IBPs. Hence, herein we apply a recently published method of matrix inversion (Karunarathne et al., 2019) to extract the currents of 29 IC IBPs with known locations from electric field change array data. These IBPs are in four series of 5 to 9 pulses from the IB stage of four separate flashes. Two of the IC flashes were previously studied by Marshall et al. (2013) and included TGF candidate IBPs, and the other two IC flashes occurred in storms studied by Karunarathna et al. (2017). After determining the IBP currents as functions of time, we model the pulses using a Modified Transmission Line (MTL) method and estimate various quantities including channel length, current propagation velocity, peak current, radiated power, and charge moment of each IBP. Modeling a series of IBPs during four flashes also allows an investigation of the earliest evolution, through the first 2 to 7 ms, of the IB pulses in these IC flashes. The current measurements allow us to associate some of the IBPs with TGFs. We also compare the series of IBPs with the model by Kostinskiy et al. (2020) for flash initiation and IBP development.

2. Data sources

For this study, E-change measurements were obtained from an array of 10 sites around the Kennedy Space Center (KSC) in Florida in 2011 using fast antenna sensors (e.g., Kitagawa and Brook, 1960). The fast antenna data ("Ch1") had bandwidth of 1.6-630 kHz, electronic decay time of 100 μ s, 0.3–0.5 Vm^{-1} background noise range, and 0.2 μ s time resolution. (See Karunarathne et al. (2013) for more information on the sensors and a map of the array sites.) Locations of the IB pulses were obtained by PBFA (Position by Fast Antenna) time-of-arrival method (Karunarathne et al., 2013). Data from the lightning mapping system called Lightning Detection and Ranging II (LDAR2), which located lightning events using VHF radio signals (within 60-66 MHz range) and a similar time-of-arrival technique (Murphy et al., 2008; Thomas et al., 2004), were used to help verify the PBFA locations for some IBPs. For comparisons of IB pulse amplitudes from different IC flashes, we "rangenormalize" the peak amplitude Emax of each IBP (at a known distance, R, in kilometers from the E-change sensor) to its amplitude at a range of 100 km as follows: $E_{100km} = E_{max} \bullet (R/100)$.

Thundercloud precipitation structure and flash event locations within the clouds were over-plotted (e.g., Karunarathna et al., 2015) using data from Next Generation Weather Radar (NEXRAD or WSR—88D) operated by the NOAA/National Weather Service. Radar data were obtained from the Melbourne (KMLB) and Tampa Bay (KTBW) stations. Especially strong lightning pulses are often located in time and space by the Worldwide Lightning Location Network or WWLLN (e.g., Hutchins et al., 2012). Most WWLLN-detected events are CG lightning return strokes, but IB pulses of some IC flashes are also detected, including a few of the IBPs studied herein. In 2010 WWLLN had location uncertainty of <10 km and event time uncertainty of <10 μ s for "most" events (Hutchins et al., 2012); it is expected that the uncertainties were at least as small for the 2011 data used in this study.

3. Method of modeling

3.1. Model basics

This study applies the same theory and modeling method, *matrix inversion*, as first described in Karunarathne et al. (2019) and used for modeling CG IBPs in Karunarathne et al. (2020). Starting from Uman et al. (1975) (adapted for short, in-cloud current pulses rather than lightning return strokes, as done by Watson and Marshall (2007) and others), the vertical electric field, E_z (D, t) at any point on a conducting plane due to an arbitrary current i(z,t) moving vertically from lower altitude H_1 to upper altitude H_2 is the sum of vertical components of electrostatic $E_e(D,t)$, induction $E_i(D,t)$ and radiation $E_r(D,t)$ electric fields, respectively, as

$$\begin{split} E_{z}(D,t) &= \frac{1}{2\pi\epsilon_{0}} \left[\int_{H_{1}}^{H_{2}} \frac{2 - 3\sin^{2}\theta}{R^{3}} \int_{0}^{t} i\left(z,\tau - \frac{R}{c}\right) d\tau dz \right. \\ &+ \int_{H_{1}}^{H_{2}} \frac{2 - 3\sin^{2}\theta}{cR^{2}} i\left(z,t - \frac{R}{c}\right) dz - \int_{H_{1}}^{H_{2}} \frac{\sin^{2}\theta}{c^{2}R} \frac{\partial i(z,t - R/c)}{\partial t} dz \right] \end{split} \tag{1}$$

where D is the horizontal distance from the channel to the observation point, the source current pulse is at altitude z at time t, $R=\sqrt{D^2+z^2}$ is the distance from the source to the observation point, c is the speed of light in air, ϵ_0 is the permittivity of free space, and the angle.

 $\theta = \cot^{-1}\left(-z/D\right)$ and is measured from zenith (or upward vertical) at the source point down to R. According to their inverse dependence on powers of R, $E_r(D,t)$ dominates for so-called 'far-field' observations (usually D>20 km). Thus, in many situations $E_z(D,t)$ for a given station (at fixed D) can be approximated as,

$$E(t) \approx \frac{-1}{2\pi\epsilon_0} \int_{H_1}^{H_2} \frac{D^2}{c^2 (D^2 + z^2)^{3/2}} \frac{\partial i(z, t - R/c)}{\partial t} dz$$
 (2)

Modified transmission line (MTL) models are commonly used to describe the current behavior of different types of lightning discharges among several other developed analytical models (Rakov and Dulzon, 1987; Shao and Heavner, 2006; Watson and Marshall, 2007; Nag and Rakov, 2010a; Zhu et al., 2010; Karunarathne et al., 2014). Rather than using a transmission line model, da Silva and Pasko (2015) modeled a CG IBP and an NBE assuming that these events were both caused by a sudden step elongation at the negative end of a bidirectional leader.

The MTL model defines the current of a discharge as traveling through a vertical conducting channel in terms of time and altitude. Hence, according to MTL models the current i(z,t) is written as the product of two terms, one depending on z, and the other depending on t and t. For this study, we use the MTLE (modified transmission line, exponentially decreasing) model for the altitude dependence of i(z,t), as it was determined to work best for most of the IBPs modeled by Karunarathne et al. (2014). When the current pulse is injected into the transmission line, the distribution of the downward moving current through the conductive channel exists from t12 to t11, and is given by

$$i(z,t) = exp\left(-\frac{|H_2 - z|}{\lambda}\right)I\left(t - \frac{H_2 - z}{\nu}\right)$$
(3)

where ν is the propagation speed of the current pulse along the transmission line and λ is the decay constant of current with altitude. Note that I on the right hand side of Eq. (3) is a different function from i(z,t).

Previous studies have used an asymmetric Gaussian shaped curve for the current behavior of small cloud discharges with time, $I(t - \frac{H_2 - z}{V})$ (e.g., Gurevich and Zybin, 2005; Karunarathne et al., 2014; Watson and Marshall, 2007). However, since the asymmetric Gaussian cannot describe complex features of IBPs such as subpulses, herein we use the matrix inversion method to extract the time derivative of current, $\partial I/\partial t$, from the *E*-change measurements using Eq. (2) and integrate to obtain $I(t - \frac{H_2 - z}{V})$, as described in section 3.2 of Karunarathne et al. (2019).

3.2. Modeling procedure

A series of IBPs from four IC flashes that occurred on 14 August 2011 at 2318:27 UT and 0030:28 UT, and on 22 July 2011 at 1705:41 UT and 1712:20 UT were studied. These IBPs were modeled with a MTLE model using the matrix inversion method to determine the IBP current. Farfield *E*-change data were taken from fast antenna measurements, and IBP locations were taken from PBFA. (Note that for each flash modeled herein, the locations of successive IBPs changed mainly in the vertical, thereby justifying our use of Eq. (1), which assumes a vertical channel.) Thus there were only three remaining parameters to find the current: vertical channel length L (where $L=H_2\text{-}H_1$), altitude decay constant (λ) of the current, and velocity (v) of the current. These parameters were determined by comparing measured and modeled waveforms, and then searching for the best fit to the measured *E*-change data.

We use the normalized fit parameter (ρ_{norm}) as developed by Karunarathne et al. (2014) to quantify how closely the modeled waveform fits with the measured E-change data.

$$\rho norm = \frac{1}{M} \sum_{i=1}^{M} \cdot \sum_{n=1}^{i} \sqrt{\frac{1}{M_{i}} \frac{\left(E_{m}^{i}(t_{n}) - E_{c}^{i}(t_{n})\right)^{2}}{\left(\Delta E_{m,p}^{i}\right)^{2}}}$$
(4)

Here, M is the total number of modeled waveforms (equal to the number of sensors with data for each IBP individually), M_i is the number of samples from ith sensor. $E_m^i(t_n)$, $E_c^i(t_n)$ are measured electric field and calculated electric field by Eq. (1) at time t_n , and $\Delta E_{m,p}^i$ is the measured peak-to-peak electric field of ith sensor. If the modeled waveform fits exactly with the measured one, then ρ_{norm} is zero. Therefore, to obtain the best model solution for each IBP, ρ_{norm} was minimized by changing the three unknown parameters (v, L, and λ) using a numerical computational method. (Note that, unlike in Karunarathne et al. (2019) where λ was a function of channel length, here we vary λ to improve the fitting.) Since ρ_{norm} could have multiple local minima on the set of free parameters, initially we used 10 equally spaced trial values for each parameter. Then the 10 parameter sets with the best (lowest p_{norm}) minima were used as starting points for another set of searches to find the global minimum of $\rho_{\text{norm}}.$ The set of free parameters which gave the smallest ρ_{norm} for each pulse was considered as the best model solution

Other electrical properties of each IBP can be found using the obtained IBP current waveform and length. From Nag and Rakov (2010b), the radiated power (P_{rad}) and total energy dissipated (W) are expressed

$$P_{rad}(t) = \frac{(H_2 - H_1)^2}{6\pi\epsilon_0 c^3} \left(\frac{d\,i(t)}{dt}\right)^2 \eqno(5)$$

$$W = \int_0^t P_{\text{rad}}(\tau) d\tau \tag{6}$$

with integration time, *t*. in Eq. (6) equal to the IBP duration. Vertical charge moment (P) and total charge (Q) for each IBP are given by the following expressions (e.g., Karunarathne et al., 2014; Nag and Rakov, 2010b):

$$P = \int_{H_1}^{H_2} \int_0^t i\left(z, \tau - \frac{R}{c}\right) d\tau \, dz \tag{7}$$

$$Q = \int_{0}^{t} i\left(z, \tau - \frac{R}{c}\right) d\tau \tag{8}$$

Karunarathne et al. (2014) used three different transmission line models to study six IBPs from CG flashes and showed that different models can give different combinations of peak current and channel length. Here we focus on two of these MTL models: MTLE with IBP current decaying exponentially with distance traveled (as used herein)

and MTLL with IBP current decaying linearly (as used in our paper on CG IBPs, Karunarathne et al., 2020). Karunarathne et al. (2014) found that the charge moment change, QL (where Q is the total charge moved by the IBP and L is the channel length), was almost identical for the different MTL models. Based on modeling of six IBPs, Karunarathne et al. (2014) found that on average the MTLE results had Q values about 1.7 times larger than MTLL results, while the MTLL L values were longer by about the same factor (1.7) than the MTLE lengths. Thus the MTLE and MTLL models agreed on QL. As discussed in Karunarathne et al. (2014), Koshak et al. (2007) modeled IC flashes as a discharge between two equal, opposite charges $(\pm Q)$ separated by a distance L and found that reasonable models all had the same value of QL, but did not necessarily agree on Q or L. Koshak et al. (2007) called this finding the "fundamental dipole ambiguity." Thus, it is not surprising that models of IBPs are subject to the fundamental dipole ambiguity, as found by Karunarathne et al. (2014), and readers should keep this ambiguity in mind.

4. Results for four IC flashes

The first two flashes studied herein have been studied by Marshall et al. (2013) to describe possible TGF occurrences during the IB stage of IC flashes; Marshall et al. (2013) described the IBPs using wideband *E*-change, multiband magnetic field change, PBFA locations, and LDAR2 VHF lightning mapping data. For these two flashes, Marshall et al. (2013) give full details on the early series of IB pulses, which include (in each flash) two very large amplitude, classic IC IBPs. The other two flashes examined herein were part of a study by Karunarathna et al. (2017) of lightning initiation locations in multiple storms on one day. We examine these last two flashes mainly for comparison because they are typical IC flashes without any very large amplitude, classic IC IBPs.

4.1. Example 1: 14 August 2011 at 2318:27 UT flash

The Example 1 IC flash occurred at a distance of about 28 km from the closest sensor, K14. Fig. 1 shows the *E*-change observations with respect to the time for the first 10 ms from the beginning of the flash at K14 site. (The E-change data are from the "Ch3" sensor, with a decay time constant of 1 s.) The PBFA locations and times for the main bipolar peak of the nine IBPs we modeled are also shown, along with the LDAR-detected events in the first 10 ms. (PBFA also located the sub-pulses of these IBPs, but for clarity we have plotted only the main IBP peaks in Fig. 1a; see Marshall et al. (2013) for the other locations.) Seven of the ten stations recorded triggered data (K02, K14, K24, K17, STC, FLT and OVD) for this flash, and all of them were in the 'far field' relative to the IBP locations. The horizontal and vertical errors of PBFA locations were both 250–450 m (Marshall et al., 2013).

The nine modeled IBPs occurred in the first 7 ms of the IB stage of this flash and are labeled as IBP 1 to 9 and color-coded in Fig. 1. As detailed in Marshall et al. (2013), the IB stage of this flash included, in sequence: intermediate IBP1, classic IBP2, intermediate IBP3, single subpulse classic IBP4, classic IBP5, three subpulse classic IBP6, two more intermediate IBPs (7 and 8), and a four subpulse classic IBP9. (Note that in this description, a "classic IBP" has no subpulses unless so noted: a "single subpulse classic IBP" has one subpulse and the main peak.) No narrow IBPs were located or modeled.

The PBFA altitudes of the modeled IBPs were 7.2–10.5 km and located in reflectivity of about 34 to 18 dBZ, as shown in Fig. 1c. Four LDAR locations during this time period (2318:27.4265–2318:27.4335 UT) were at 11.3–12.8 km altitude, in radar reflectivity of 20 to 10 dBZ. As described in Marshall et al. (2013) and supported by the data in Fig. 1, the PBFA locations of the first nine IBPs extended upward about 3200 m from its initiation near 7.3 km to to 10.5 km.

Fig. 2a shows an example of modeling an IBP: the modeled IBP6 fits well with the IBP6 *E*-change data at all seven sensor sites. Note that the current amplitude is not an adjustable parameter in the matrix inversion modeling (it varies as the three unknown parameters (v, L, and λ) are

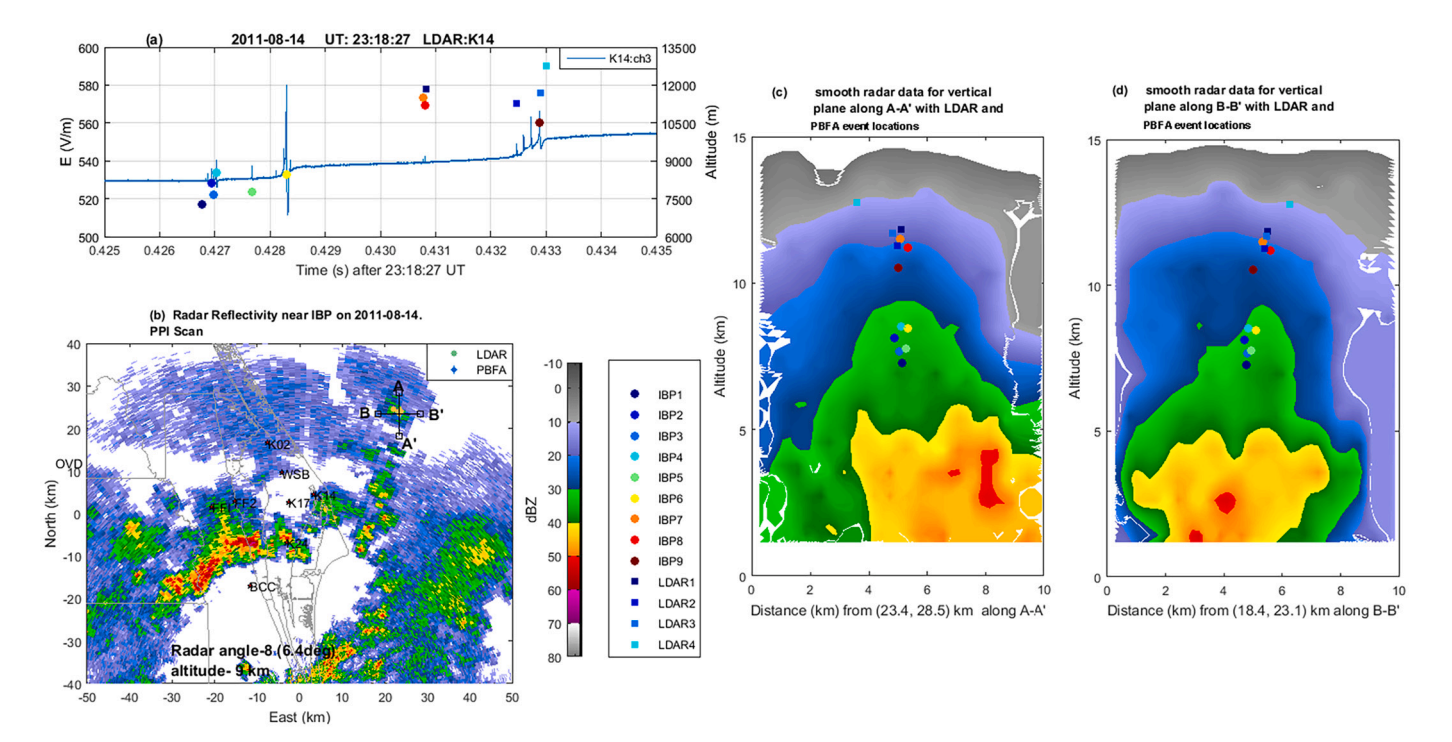


Fig. 1. (a) *E*-change data and IBP altitudes for the first 10 ms of Example 1. Time period of data shown is 2318:27.425–2318:27.435 UT. Each modeled IBP (IBP1 - IBP9) was located with PBFA, shown as colored circles; LDAR locations are colored squares. (b) Reflectivity from Plan Position Indicator (PPI) scan (beam angle 6.4° , \sim 9 km altitude at range to IBPs, shown overlaid) at 2315 UT, from KMLB radar. Sensor sites are indicated by three-letter identifiers. (c) Vertical cross section along A-A', North-to-South, with PBFA and LDAR locations projected onto plane. (d) As in Fig. 1c except showing West-to-East vertical cross section along B-B' through IBPs.

varied); instead the determination of $\partial i/\partial t$ from the calibrated E-change data at multiple sensor sites leads to the IBP current waveform, including its peak current when $\partial i/\partial t$ is time integrated. The best value of ρ_{norm} is 0.008, given by average propagation velocity (v) of 18×10^7 m/s, vertical length (L) of 875 m, and λ (exponential decay length of the current) is 495 m. The resulting peak current (I $_p$) is -270 kA, which would be considered large even for a CG return stroke. The charge moment (P) of the pulse was -3451C m and the total charge (Q) was -8.4C.

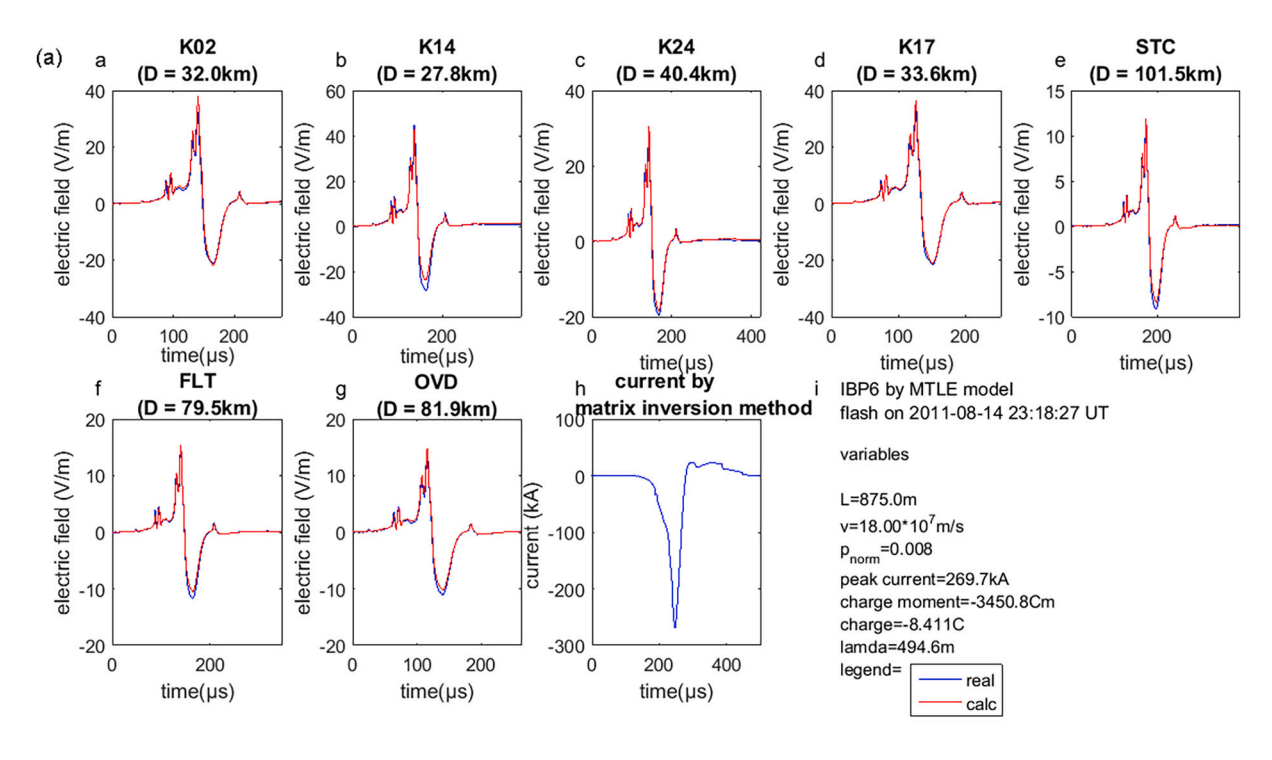
Fig. 2b displays the modeled current of IBP6, along with the resulting E-change calculated from the model, at the K14 observation site. IBP6 has a total duration of about 150 µs with three subpulses on the rising side of the main bipolar pulse (and is followed immediately by a single pulse). The IBP6 current is almost an asymmetric Gaussian shaped curve with a rise time (time taken to increase to 90% of peak current from 10% of peak current) of 53 µs and a fall time (time taken to reduce current to 10% of the peak from the increasing 90% of peak current) of 34 μs. This finding is unusual since, as shown below, most IBP currents in the four IC flashes studied herein have significantly slower fall times than the rise times. Also in Fig. 2b, we observe that the current of IBP6 is not uniformly rising to the peak. The derived current of IBP6 has three 'humps' on the rising section, where the current briefly undergoes a steeper increase. Each of these humps occurs at the time of a subpulse in the Echange data, indicating that the current humps are causing the subpulses. Hence, we can conclude that the subpulses on this complicated IBP appear to be due to individual current pulses, each adding to the main current.

As described in Marshall et al. (2013) and shown in Fig. 1a, about 2.4 ms after IBP6 there were two single-pulse IBPs with small amplitudes, IBP7 and IBP8. About 1.6 ms after IBP8, IBP9 occurred. This pulse had a 600 μs duration, and according to PBFA locations, it spanned about 1.0 km in altitude. The model results for IBP9 are shown in Fig. 3a for all seven sites. The best value of the ρ_{norm} is 0.020, with velocity of 17.3 $\times 10^7$ m/s, length of 793 m, and λ of 172 m. Like IBP6, IBP9's

length, peak current, charge moment, total charge, peak radiated power, and total energy dissipated are all unusually large, especially the charge moment, —4524C m, and the total charge, —26.5C. An alternate interpretation of IBP9 is that it consisted of a group of four classic IBPs in the 600 μs , rather than one IBP with a duration of 600 μs , since such a long IBP duration is without precedent. In this group, successive IBPs are separated by 110, 120, and 120 μs , and the four IBPs have durations of 22, 20, 52, and 95 μs . We will continue referring to this group of IBPs as IBP9 while recognizing that it consists of four classic IBPs that we label IBP9a, IBP9b, IBP9c, and IBP9d. The modeling calculates the various parameters for the entire IBP9 waveform; only for peak current do we estimate the individual currents from the modeled current waveform.

Fig. 3b shows the IBP9 current pulse obtained from the model and the reproduced E-change curve at site K14. Within IBP9, IBP9a, IBP9b, IBP9c, and IBP9d have peak currents of 35, 75, 217, and 190 kA, respectively. The overall peak E-change amplitude at 100 km of IBP9 was 4.8 V/m. Within IBP9 the E-change amplitude of each successive classic IBP increased. As shown in Fig. 3b, the current variation in time is similar to but more complicated for IBP9, with its rapid succession of separate IBPs, than for IBP6, with its relatively small subpulses. Overall, the IBP9 current shows well-defined humps on the main pulse with a longer rise time (259 µs) than fall time (201 µs). By looking at how changes in the current coincide with each of the four classic IBPs of IBP9, we see that a rapid sequence of large current pulses cause the IBPs. The current reaches its peak value with the third IBP, although the fourth IBP has a slightly larger E-change peak at most of the sensor sites. The complicated IBP9 current shape is unique among the 29 IBPs investigated herein, but it easily fits with the idea that IBP9 is a group of four classic IBPs in rapid succession.

Note that the IBP current in Fig. 3b becomes positive for the last 200 μ s after IBP9d. This positive current is an artifact caused by two factors: the long duration of IBP9d (95 μ s) combined with Ch1 fast antenna data having an exponential decay time constant of 100 μ s. In Fig. 3b, starting at t \sim 640 μ s there is a decrease in E-change that results



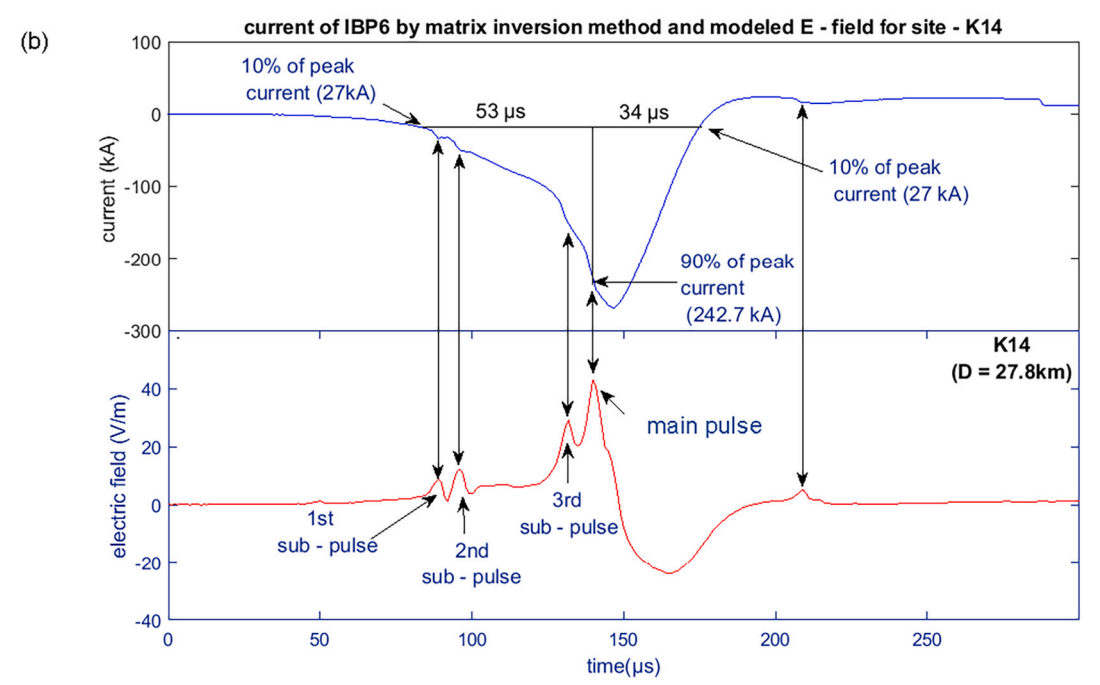


Fig. 2. Model results for IBP6 of Example 1 IC flash. (a) Panels a - g are measured E-change data at K02, K14,K24, K17, STC, FLT and OVD sites, overlaid with the calculated pulse using the modeled current shape as determined from matrix inversion method. Values above each plot give the horizontal distance (D) from the IBP to each site. Panel h is derived current with respect to time for IBP6, and panel i lists the calculated parameters. (b) Expanded view of derived current (time shifted to K14) with its calculated field at K14 site. Time correspondence between 'humps' in current and subpulses in E-change are indicated with double-ended vertical arrows. The 10-to-90% risetime and falltime are given; peak current value is 269.7 kA.

from the sensor's electronic decay; this decrease is seen at all seven sensors in Fig. 3a. This artificial decrease causes the matrix inversion technique to determine an artificial positive current. Most IBPs modeled herein have durations well less than 100 μs , so the electronic decay does not "produce" artificial positive currents at the end of those IBPs. However, a few IBPs shown later also end with positive currents that are artifacts. For comparison, Fig. 1a shows the "Ch3" data (decay time constant of 1 s) with no sensor electronic decay occuring in the 600 μs

duration of IBP9 (see also Fig. 5 in Marshall et al. (2013)).

All obtained characteristics of the nine modeled IBPs of Example 1 along with the minimum, maximum, and average values and standard deviations are listed in Table 1. Range normalized *E*-change amplitude varied from 0.2 to 12.6 V/m (average 2.7 \pm 4 V/m); IBP6 and IBP9 were the only two IBPs that exceeded the average value, and both these had E-change values that were more than twice as large as any other pulses. The current rise times of the IBPs ranged from 2 to 259 μs with a mean of

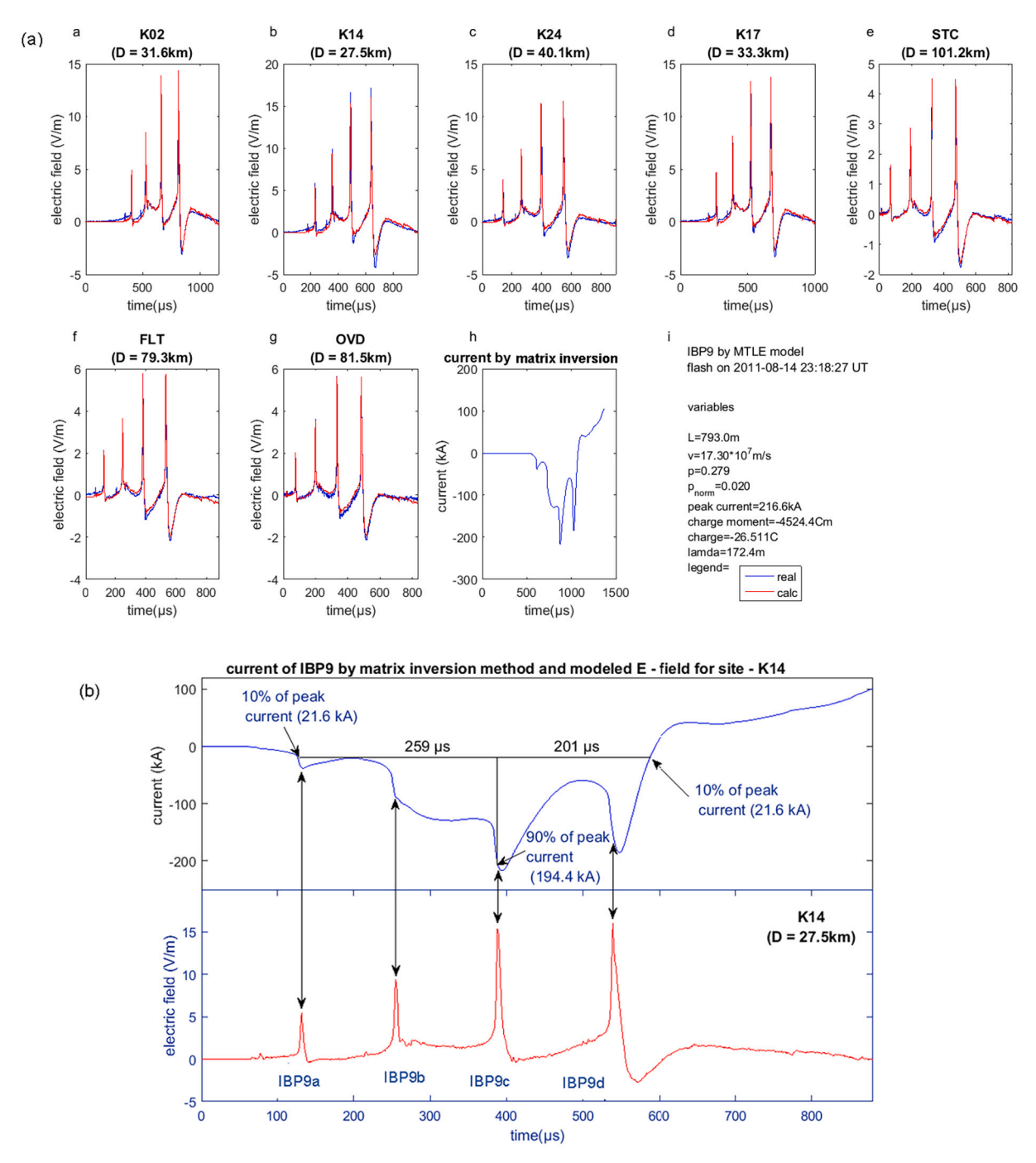


Fig. 3. As in Fig. 2, except showing IBP9 of Example 1. (a) Measured and calculated E-change values, along with derived parameters for the best-fit result (lower right, panel i). (b) Derived current (time shifted to K14) and calculated electric field at K14 site.

 $(41.9\pm83~\mu s)$, and fall times ranged from 12 to 201 μs with a mean of $(46.2\pm58.7~\mu s)$. Unlike CG IBPs studied previously (e.g., Karunarathne et al., 2020) and unlike the other 7 IC IBPs of this flash, IBP6 and IBP9 had longer rise times than fall times. (Note that the last four lines of Table 1 give the minimum, maximum, and average values and standard deviations of parameters for seven IBPs excluding IBP6 and IBP9.)

Length of the conducting channel and velocity of the current varied between 150 and 875 m and $11.6\text{--}18\times10^7$ m/s respectively. IBP5, IBP7 and IBP8 had the smallest lengths and velocities, while IBP6 and IBP9 had the largest values of these parameters. In general, the modeled current length of each successive IBP was approximately the same as the vertical distance between that IBP and the previous IBP (based on PBFA locations). This is unlike the lengths of IBPs in CG flashes studied by

Karunarathne et al. (2020), which extended from each IBP location all the way back (up) to the flash initiation point. However, the CG IBP lengths were determined from high speed video data, rather than determined from the modeling. Further, since the length of each CG IBP was known, Karunarathne et al. (2020) modeled CG IBPs using matrix inversion with a MTLL (modified transmission line, linearly decaying). Herein we use MTLE (exponentially decaying), which would emphasize the earlier (upper) part of the IBP current length. Overall, these results for the series of IC IBPs indicate that the apparent vertical length determined from the modeling is about the same as the new addition to the upward-extending initial leader associated with each new IBP.

Further support for the above finding that the current of most or all IBPs do not extend into the previous IBPs is found in their exponential

Table 1Obtained electrical and physical properties of Example 1 IBPs.

IBP number	Rise time (μs)	Fall time (µs)	Peak E at 100 km (V/ m)	Vertical length (m)	Velocity (10 ⁷ m/s)	Lambda (m)	Peak current (kA)	ρ norm (10 ⁻²)	Charge moment (C m)	Total charge (C)	Peak radiated power (GW)	Total energy dissipated (kJ)
1	9	32	0.5	290	15.4	31.5	22.0	3.2	-13.0	-0.41	1.7	2.9
2	6	12	1.2	429	16.1	55.9	29.1	2.3	-14.3	-0.26	8.0	12.8
3	2	19	0.7	430	11.7	84.1	13.7	3.6	-17.9	-0.21	3.8	6.4
4	22	34	2.3	512	14.4	66.8	135	1.8	-204	-3.05	21.8	135.3
5	18	39	1.5	461	11.6	50.1	76.3	1.4	-92.3	-1.84	12.2	38.2
6*	53	34	12.6	875	18.0	494.6	270	0.8	-3451	-8.41	64.0	789.4
7	3	20	0.2	175	15.0	15.2	17.6	4.9	-3.0	-0.20	0.5	1.3
8	5	25	0.5	150	16.5	26.0	22.1	3.2	-8.2	-0.32	0.6	1.0
9*	259	201	4.8	793	17.3	172.4	217	2	-4524	-26.51	37.5	487.1
min	2	12	0.2	150	11.6	15.2	13.7	0.8	-3.0	-0.20	0.5	1.0
max	259	201	12.6	875	18.0	494.6	270	4.9	-4524	-26.51	64.0	789.4
avg	41.9	46.2	2.7	457	15.1	110.7	89.1	2.6	-925.3	-4.58	16.7	163.8
std	83	58.7	4	249	2.3	151.3	96.5	1.3	1758	8.6	21.5	282.6
min	2	12	0.2	150	11.6	15.2	13.7		-3.0	-0.20	0.5	1.0
max	22	39	2.3	512	16.5	84.1	135		-204	-3.05	21.8	135.3
avg	9.3	25.9	1.0	349.5	14.4	47.1	45.1		-50.3	-0.9	6.9	28.3
std	7.7	9.6	0.7	144.5	2.0	24.3	44.8		74.2	1.1	7.8	49.0

Notes: IBPs marked with * are 'extraordinary' pulses. These are removed from the set in determining statistical values in the lowest four rows (*).

decay constant, λ . Specifically, if λ is much smaller than the IBP vertical length, then the IBP current essentially dies out before the full modeled vertical length has been traversed. Table 1 shows that for IBPs in Example 1, the average λ was 111 m while the average vertical length was 457 m, so on average the vertical IBP length contained 4.12 decay constants. Since the current amplitude declines by 1/e for each λ , at the bottom of the average IBP length the current amplitude will have fallen to only 1.6% of the peak current value. If the vertical length equals 5λ , then the current will be 0.7% of the peak current. Thus, any additional IBP length beyond 5λ will be carrying almost no current. As seen in Table 1, several IBPs had lengths of more than 5λ. IBP1 of Example 1 had a modeled vertical length of 290 m and λ of 31.5 m for a total length of about 9λ; thus, one might conclude that the vertical length of IBP1 with significant current was only 5λ or 158 m. We have chosen not to shorten the vertical IBP lengths displayed in Table 1 since they were determined by our modeling, but the above calculations indicate that the vertical lengths resulting for some IBPs might be considered longer than

The peak current magnitude varied from 14 to 270 kA, the peak radiated power ranged from 0.5 to 64 GW, and the total energy dissipated ranged from 1 to 790 kJ. The maximum values of peak current, peak radiated power and total energy dissipated were found with IBP6 and IBP9, while IBP3, IBP7 and IBP8 had the smallest values. Magnitudes of the corresponding total charge and charge moment ranged over 0.2–26.5C and 3–4524C m, respectively. IBP7 and IBP8 had the smallest charge moment magnitudes, and the total charge of these two was small like that found for the first three IBPs. In contrast, IBP6 and especially IBP9 had substantially larger magnitudes of charge and charge moment compared to all the other pulses.

Fig. 4 summarizes the model results for Example 1. Upper panels show an overlay comparison of modeled IBPs on the measured IBPs, the shape and magnitude of each IBP modeled current, and the corresponding radiated power of each IBP. Fig. 4 also shows how other parameters vary with each pulse. Generally, peak currents, propagation velocities, channel lengths, total charges, charge moments, peak radiated powers and total energy dissipated all varied directly with the peak *E*-change amplitude (that is, larger values with greater E-change peak and smaller values with smaller *E*-change peak). In the first 1.5 ms of this flash the succession of vertical length results during the series of IBPs 1–6 indicates increasing lengths until something unexpected occurs during or after IBP6. There is a long 2.4 ms pause before IBP7, and the current lengths of IBP7 and IBP8 are much shorter than any earlier pulses. We hypothesize that after IBP6 the initial leader took a relatively long time to reach the altitude where the next IBPs could occur. This

notion fits with the altitude data from PBFA and LDAR (Fig. 1), showing a nearly 2 km gap between IBPs 1–6 and IBPs 7–9. An alternative hypothesis is that the flash stopped developing after IBP6, paused, then restarted just before IBP7. We describe how this restarting might happen below (Section 5), after discussing a possible physical mechanism for IBPs

As listed in Table 1, we also see in Fig. 4 that both IBP6 and IBP9 had very large values of most of the modeled parameters compared to the other IBPs in the flash. Overall, IBP6 and IBP9 are clearly outliers in this flash, with their E-change waveforms yielding modeled peak current magnitudes in excess of 200 kA, vertical lengths of ~800 m, and charge moments of 3500–4500C m. Their peak radiated powers, 64.0 and 37.5 GW, and their total dissipated energies of 789.4 and 487.1 kJ, are substantial, likely making them detectable at great ranges in various electromagnetic frequency bands. Hence, we consider IBP6 and IBP9 to be "extraordinary" IBPs because, compared to the other IBPs, their lengths, peak currents, charge moments, total charges, peak radiated powers, and total energies are all unusually large.

One goal of this study is to learn more about how TGFs are produced by IC flashes (despite our having no detections of TGFs due to lack of suitable instrumentation). It seems likely that the extraordinary IBP6 and IBP9 may have been associated with TGFs, as hypothesized in Marshall et al. (2013). The fact that there was a WWLLN-detected event (with an energy of 5000 J in the 5–18 kHz band) coincident with IBP6 further supports the possibility that IBP6 caused a TGF, since Connaughton et al. (2013) have found that 10–50% of TGFs seen by the Fermi satellite had coincident WWLLN events (with the higher percentage associated with the shortest TGFs).

There is a second, stronger fact that supports a TGF association for IBP6, as well as for IBP9c and IBP9d. Lyu et al. (2016) showed that an "Energetic IC Pulse" or EIP is likely the radio signal of a TGF event. The main EIP characteristics are a pulse occurring within the first few milliseconds of an IC flash, located between 8 and 13 km altitude, and having a peak current magnitude >150 kA with a relatively long duration (mean of 55 µs and range of 40–100 µs for main pulse) (Lyu et al., 2015, 2016). Based on our modeling and measurements, IBP6 fits the EIP characteristics: its peak current magnitude is 270 kA, the main pulse duration is about 60 µs, and it occurred 1.4 ms after the beginning of the IC flash at an altitude of 8.4 km. IBP9c and IBP9d also fit the EIP characteristics with peak currents of 217 and 190 kA, main peak durations of 42 and 95 μ s, altitudes of 11.5 and 10.5 km, and occurrence times about 5.8 ms after the beginning of the flash. Thus, it seems likely that IBP6, IBP9c, and IBP9d in Example 1 were associated with three separate TGF events.

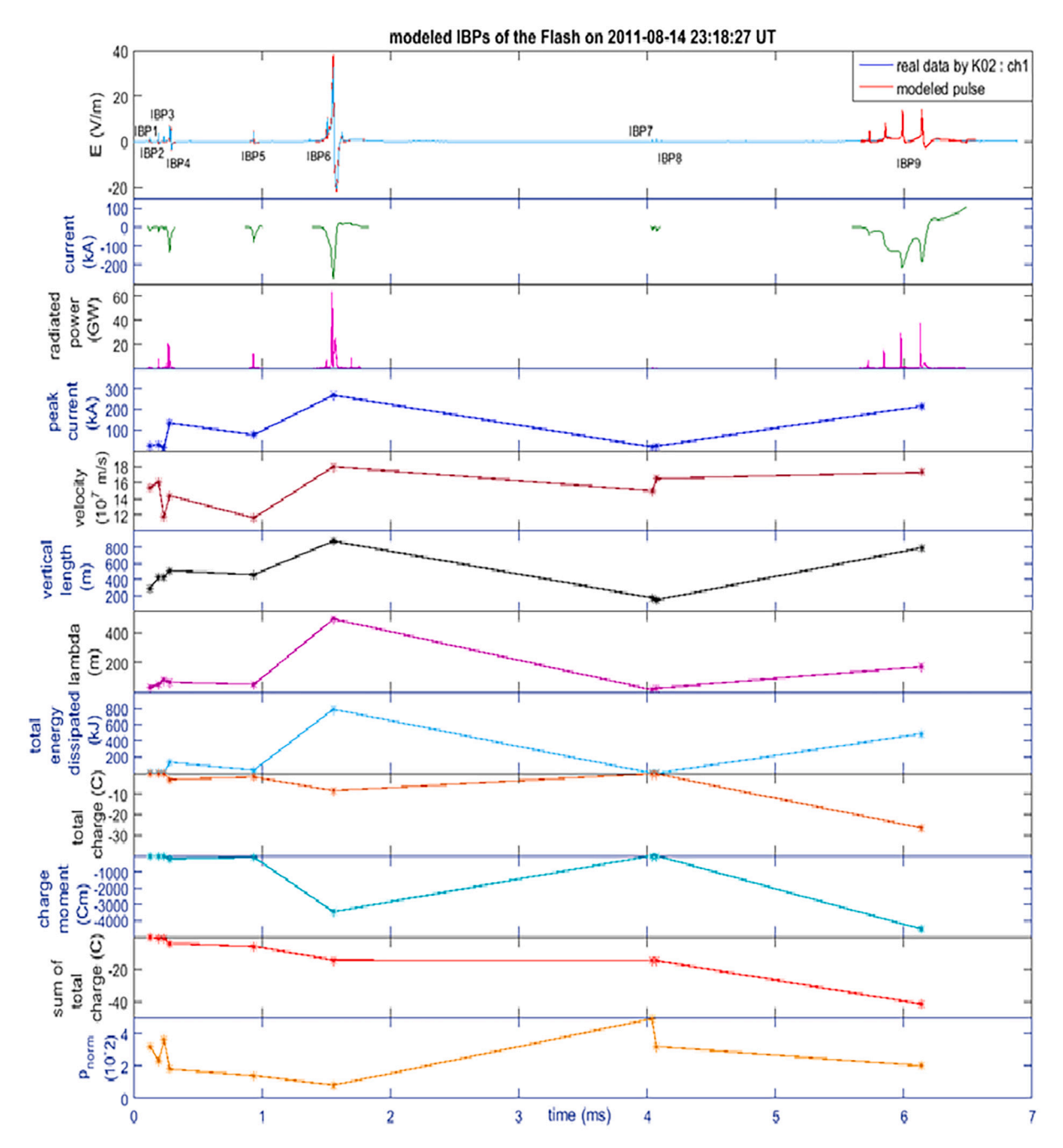


Fig. 4. Summary of model results for nine IBPs in the first 7 ms of Example 1 flash, 14 August 2011, 2318:27 UT. Top panel is measured E-change data during the IB stage (at K02 site) and each of the nine modeled IBPs.Lower eleven panels show model results for each IBP: current, peak current magnitude, radiated power, propagation velocity, vertical length, lambda, total energy dissipated, total charge, charge moment, sum of total charge, and ρnorm of best fitting model results.

4.2. Example 2: 14 August 2011 at 0030:28 UT flash

The Example 2 IC flash initiated 22.2 km away from the closest sensor, FLT. The IB stage had eight IBPs within the first 7 ms, and they spanned nearly 4.7 km vertically, starting from 7.6 km (Marshall et al., 2013). Herein, we model the first 6 ms with three intermediate IBPs and five classic IBPs distributed as follows: single subpulse classic IBP1, classic IBP2, classic IBP3, intermediate IBP4, intermediate IBP5, intermediate IBP6, four subpulse classic IBP7, and four subpulse classic IBP8; see Fig. 5a. As noted in Marshall et al. (2013) the *E*-change waveform of the IBPs and entire IB stage of this flash were similar to those of Example 1. (These two flashes occurred in the same region on the same day, but they were nearly 23 h apart and not in the same storm system.) In

particular, IBP7 and IBP8 in Example 2 are extraordinary IBPs because the same physical parameters are again unusually large (see Table 2) as found for the extraordinary pulses IBP6 and IBP9 in Example 1.

The PBFA altitudes of the modeled IBPs were 7.6–12.3 km and located in reflectivity of about 35 to 25 dBZ, as shown in Fig. 5c. Six LDAR events were located during this time period of the IB stage (0030:28.812 – 0030:28.824 UT), between 6.0 and 13.3 km altitude. As was the case for Example 1, the initial leader of Example 2 moves mainly upward, in agreement with initiation above a negative charge region and negative leader propagation toward a positive charge region (e.g., Coleman et al., 2003).

Fig. 6 shows values from the model compared to the data for IBP7 and IBP8 of Example 2. The modeled *E*-change curves fit the data well

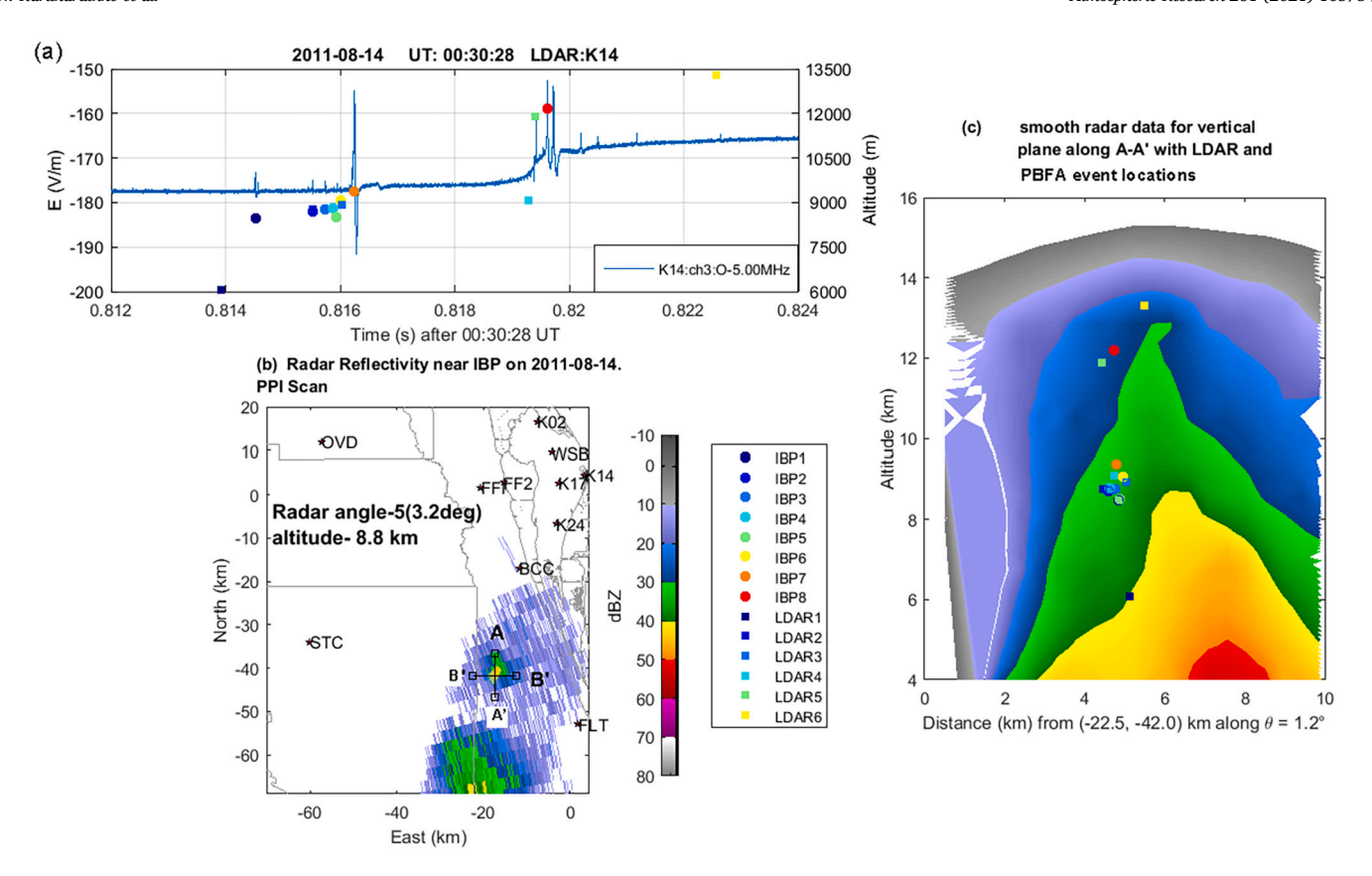


Fig. 5. As in Fig. 1, except showing data for Example 2, 14 August 2011, 0030:28 UT. (a) First 12 ms of E-change data and altitudes of modeled IBPs (IBP1–8) and LDAR sources vs time. (b) PPI of reflectivity, from KTBW radar, at scan angle near altitude of IBPs in the storm. (This storm was too close to be scanned at high altitude by KMLB radar.) Cross-section location A-A' through sources is shown. (c) North-to-south crosssection (along A-A') of reflectivity with PBFA and LDAR locations projected. Lower portions of reflectivity data are missing (below lowest scan angle at this range).

Table 2Obtained electrical and physical properties of Example 2 IBPs.

IBP number	Rise time (μs)	Fall time (µs)	Peak E at 100 km (V/ m)	Vertical length (m)	Velocity (10 ⁷ m/s)	Lambda (m)	Peak current (kA)	ρ norm (10 ⁻²)	Charge moment (C m)	Total charge (C)	Peak radiated power (GW)	Total energ dissipated (kJ)
1	13	61	1.8	260	12.3	141.3	61.0	1.4	-213	-1.80	1.4	6.6
2	6	36	0.6	110	9.2	23.9	44.6	2.8	-22.1	-0.93	0.5	1.4
3	18	28	0.9	479	14.3	104.1	19.2	2.4	-39.9	-0.39	2.8	4.2
4	10	21	0.3	90	3.8	19.6	26.7	4	-5.7	-0.29	0.2	0.4
5	5	24	0.3	379	20.6	82.5	4.7	6	-5.6	-0.07	0.2	0.4
6	1	22	0.2	286	10.5	24.9	6.8	7.3	-1.6	-0.07	0.4	0.6
7 *	49	42	10.7	1059	18.4	460	333	1.3	-6638	-16.03	60.1	1405.6
8*	234	178	9.8	1300	12.2	282.6	359	3.5	-20,055	-71.68	184.6	2674.3
min	1	21	0.2	90	3.8	19.6	4.7	1.3	-1.6	-0.07	0.2	0.4
max	234	178	10.7	1300	20.6	460	359	7.3	-20,055	-71.68	184.6	2674.3
avg	42.0	51.5	3.1	495.4	12.7	142.4	106.9	3.6	-3372.6	-11.4	31.3	511.7
std	79.0	52.8	4.5	445.7	5.3	155.2	148.9	2.1	7124.4	25.0	65.3	1002.4
min	1	21	0.2	90	3.8	19.6	4.7		-1.6	-0.07	0.2	0.4
max	18	61	1.8	479	20.6	141.3	61.0		-213	-1.8	2.8	6.6
avg	8.8	32.0	0.7	267.4	11.8	66.1	27.2	4.0	-48.1	-0.6	0.9	2.3
std	6.1	15.2	0.6	150.9	5.6	51.0	22.1		82.3	0.7	1.0	2.6

Notes: IBPs marked with * are 'extraordinary' pulses. These are removed from the set in determining statistical values in the lowest four rows (*).

 $(\rho_{norm}$ of 0.013 and 0.035) at all seven sites, at distances of 22.2 to 67.2 km. The resulting current waveforms for these two IBPs are also shown, with peak currents in excess of 300 kA and current rise times that are longer than fall times. In IBP7 (Fig. 6a) the four subpulses are relatively small compared to the main pulse, and the relatively smooth current has its peak (333 kA) coincident with the main E-change peak, even though the fourth subpulse was after the main peak. The duration of IBP7 was 130 μs .

The E-change waveform of IBP8 yields a more complicated current

waveform (Fig. 6b) with a very long duration (510 μs), similar to IBP9 of Example 1. As in Example 1, we consider IBP8 to consist of three IBPs: classic IBP8a, two subpulse classic IBP8b, and classic IBP8c. We refer to this group of three IBPs as IBP8; in this group, successive IBPs are separated by 140 and 60 μs , and IBP8a, IBP8b, and IBP8c have durations of 39, 98, and 120 μs . In Fig. 6b the peak current is coincident with the main E-change peak (IBP8b). The peak currents of IBP8a, IBP8b, and IBP8c were 160 kA, 359 kA, and 280 kA.

Overall for IBP7 and IBP8, the modeled current yielded $\,-\,16C$

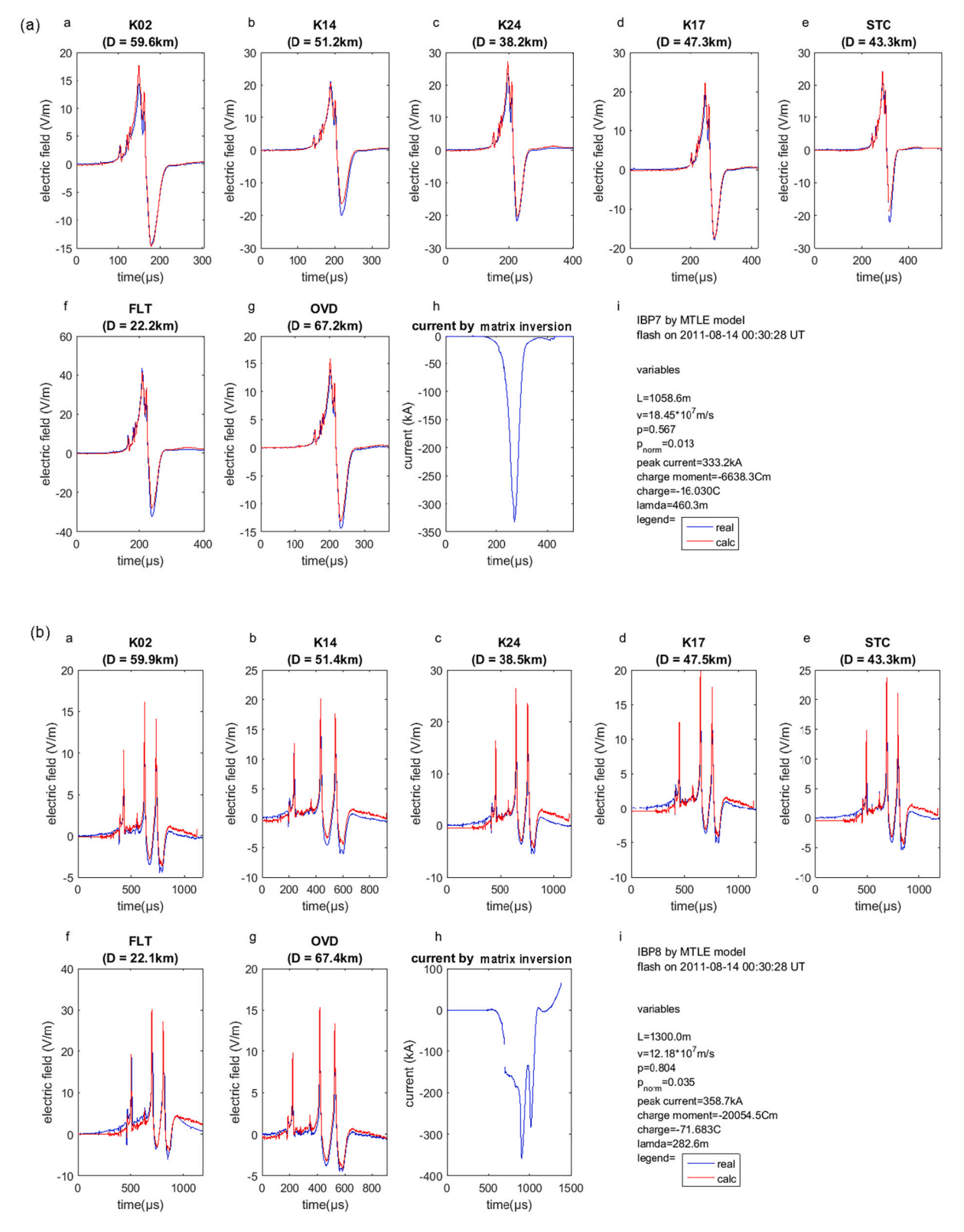


Fig. 6. Model results for two extraordinary IBPs in Example 2 IC flash. (a) As in Fig. 2a, except for IBP7 of Example 2 flash. (b) As in Fig. 2a, except for IBP8 of Example 2.

and $-\,72\mathrm{C}$ of charge transferred. Lengths for their best-fit solutions were 1059 and 1300 m, hence their charge moment magnitudes are very large, 6.6 and 20.0C km. The resulting total energy dissipated by these two pulses is 1406 and 2674 kJ, and their peak radiated powers are 60 and 185 GW, all characteristics which should make them readily

detectable in many frequency bands. Thus, in the same ways as detailed above for IBP6 and IBP9 of Example 1, IBP7 and IBP8 are extraordinary IB pulses.

Like IBP6 and IBP9 of Example 1, IBP7 and IBP8 may also have been associated with TGFs, as hypothesized in Marshall et al. (2013), though

no TGFs were detected due to lack of suitable instrumentation. There was a WWLLN-detected event coincident with IBP7 (with an energy of about 5000 J). Furthermore, IBP7, IBP8a, IBP8b, and IBP8c were probably associated with TGFs since they have the characteristics of EIPs: all had peak currents >150 kA, all occurred within 6 ms of the beginning of the flash at altitudes of 9.4, 11.6, 12.2, and 11.6 km, respectively, and the main pulse durations (85, 36, 78, and 70 μ s) are in the range given by Lyu et al. (2015) for EIPs.

Table 2 lists calculated parameters of each modeled IBP of Example 2, along with minimum, maximum, average and standard deviation of the parameters. Fig. 7 shows the value of each parameter with corresponding IBP in the series. IBP6 had the minimum current rise time

(1 µs) and IBP4 had the shortest fall time (21 µs) while IBP8 had the maximum rise (234 µs) and fall (178 µs) times. Average rise time of these nine IBPs was (42 \pm 79 µs) while average fall time was (51.5 \pm 52.8 µs). As in Example 1, rise times were longer than fall time for the two extraordinary IBPs, IBP7 and IBP8, while the first six IBPs had longer fall times than rise times. Other calculated parameters of IBP7 and IBP8, except for the current velocity, also were larger than found for the other pulses. The current velocity in IBP4 was the slowest (3.8 $\times 10^7$ m/s) and that in IBP5 was fastest (20.6 $\times 10^7$ m/s). Range normalized peak E-change varied from 0.2 V/m (IBP6) to 10.7 V/m (IBP7). Length of the conducting channel, peak current, charge moment, total charge, peak radiated power and total energy dissipated ranged as 90–1300 m,

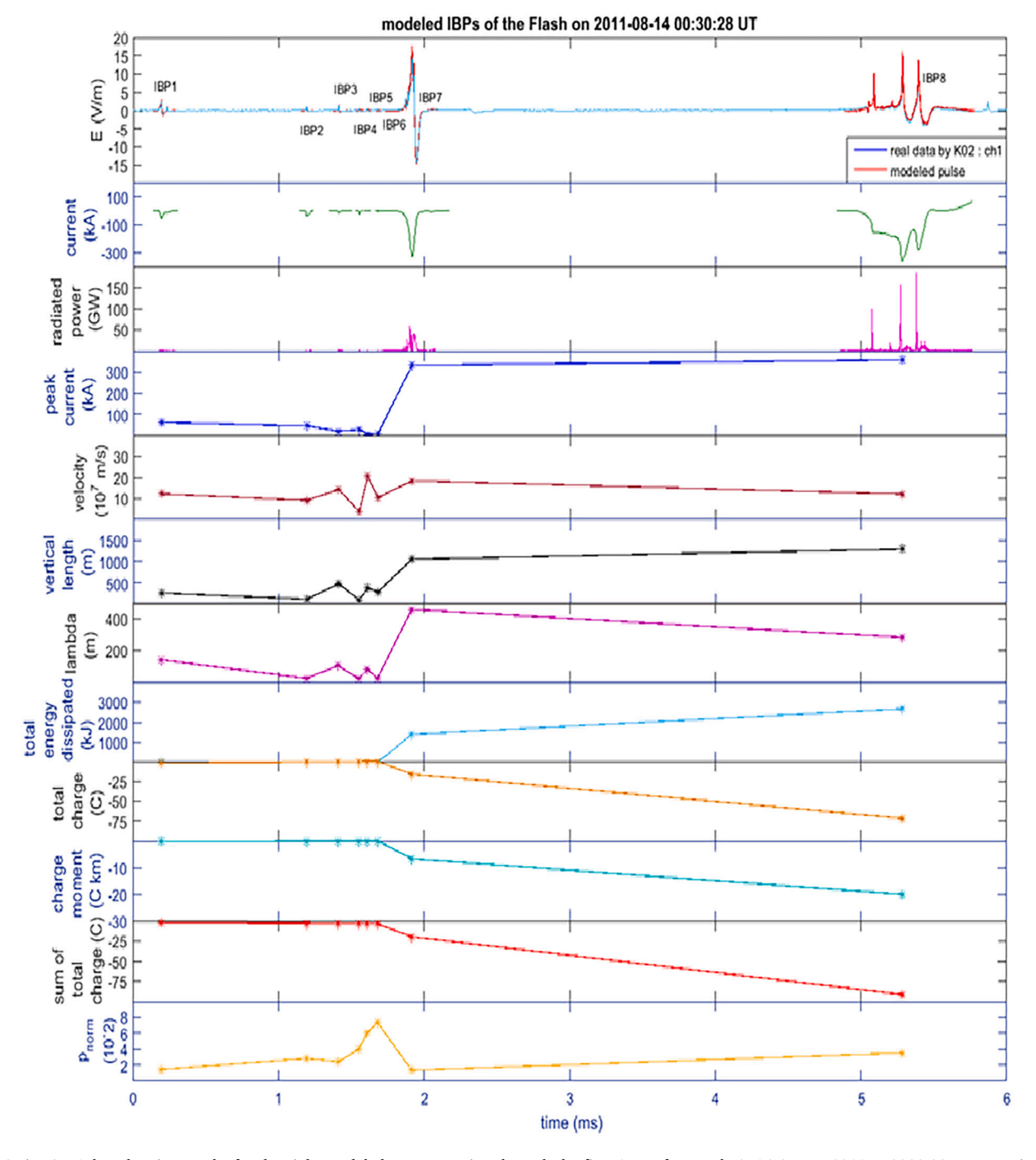


Fig. 7. As in Fig. 4, but showing results for the eight modeled IBPs occurring through the first 6 ms of Example 2, 14 August 2011 at 0030:28 UT. Data in the top panel are from at K02 site, compared to E-change values resulting from the modeling.

4.7–358.7 kA, 1.6–20,055C m, 0.1–71.7C, 0.2–184.6 GW and 0.4–2674.3 kJ. Maxima of these parameters were given by IBP7 and IBP8 while minima belong to IBP4, IBP5, and IBP6. (Note that the last four lines of Table 2 give the minimum, maximum, and average values and standard deviations of parameters for the first six IBPs, not including IBP7 and IBP8.)

As in Example 1, the model results indicate that each successive IBP conducting channel length was close to the vertical extension length of the IBP from the prior IBP, as determined from the PBFA locations. The current lengths of IBP7 and IBP8 are much longer than any of the earlier pulses, although their current velocities (18.4 and 12.2×10^7 m/s) are not extreme values. Also as in Example 1, after the extraordinary IBP7 there was a relatively long delay before IBP8 occurred, and we again hypothesize that the initial leader took a long time to reach the altitude where IBP8 could occur. This hypothesis fits with the data from PBFA and LDAR (Fig. 5), showing at least a 2 km gap in altitude between IBPS 1–7 and IBP8. As in Example 1, an alternative hypothesis is that the flash stopped developing after IBP7, then restarted just before IBP8.

4.3. Example 3: 22 July 2011 at 1705:41 UT flash

We studied seven classic IBPs in the first 4 ms of an IC flash that occurred on 22 July 2011 at 1705:41 UT (Fig. 8a). This IB stage was only about 7.1 km from the closest sensor (K17). According to PBFA locations shown in Fig. 8a and c, during the first 4 ms the initial leader propagated upward about 1.3 km vertically, starting from 6.3 km. Radar reflectivity in the region of the modeled IBPs, shown in Fig. 8c, ranged from about 20 dBZ to 10 dBZ. Seven LDAR locations were recorded in the IB stage within the same radar reflectivities, with altitude range 6.7 km up to 7.9 km. There were no WWLLN events detected with this flash.

The modeled series of IBPs consists of three classic IBPs with four subpulses (IBP1, IBP4 and IBP5), three classic IBPs with two subpulses

(IBP2, IBP3 and IBP6), and one classic IBP (IBP7). Resulting *E*-change values from the modeling along with the observed E-change data at five sensors sites are shown in Fig. 9 for IBP3 and IBP7. Importantly for this flash, only two sensors were in the far-field region, and these were used to derive the current. Despite this limitation, the matrix inversion technique is capable of finding reasonable fit to the data at all the sensors, as can be seen in Fig. 9. For IBP3, the best value of ρ_{norm} is 0.028, with v of 9.2 $\times 10^7$ m/s and L of 195 m; for IBP7, ρ_{norm} is 0.025, with v of 13.1 $\times 10^7$ m/s and L of 421 m. These values are similar to those for similarly sized pulses in Examples 1 and 2 (e.g., IBP1 in Tables 1 and 2) where more data were available to derive the current waveform.

Obtained parameters of each modeled IBP in Example 3 are shown in Fig. 10 and listed in Table 3. There were no extraordinary IBPs in Example 3. However, IBP3 and IBP4 have three of the four EIP characteristics: peak currents >150 kA, IBPs occurred within 6 ms of the beginning of the flash, and the main pulse durations (34 and 40 µs) fall in the range shown by Lyu et al. (2015). However, IBP3 and IBP4 occurred at altitudes of 6.7 km and 7.1 km, well below the minimum altitude of about 8 km for documented EIPs (Lyu et al., 2015, 2016), so it is not clear whether they should be classified as EIPs. Table 3 includes minimum, maximum, average, and standard deviation of each of the parameters for the modeled IBPs in this flash. IBP1 had the minimum peak E-change (0.5 V/m), propagation speed $(7.1 \times 10^7 \text{m/s})$, channel length (38 m), charge moment (26.6C m), peak radiated power (0.3 GW) and total energy dissipated (0.6 kJ); IBP7 had the minimum peak current (34.8 kA) and total charge (0.34C), with the maximum channel length (421 m). IBP4 had the maximum current rise time (64 µs, longer than its fall time), and also had the maximum peak current (188.7 kA), peak radiated power (7.2 GW) and total energy dissipated (35.3 kJ); however, IBP3 was the largest in peak E-change value (1.9 V/m), charge moment (283.4C m) and total charge (4.68C). IBP5 had maximum velocity $(15.9 \times 10^7 \text{ m/s})$ with second longest channel length (310 m).

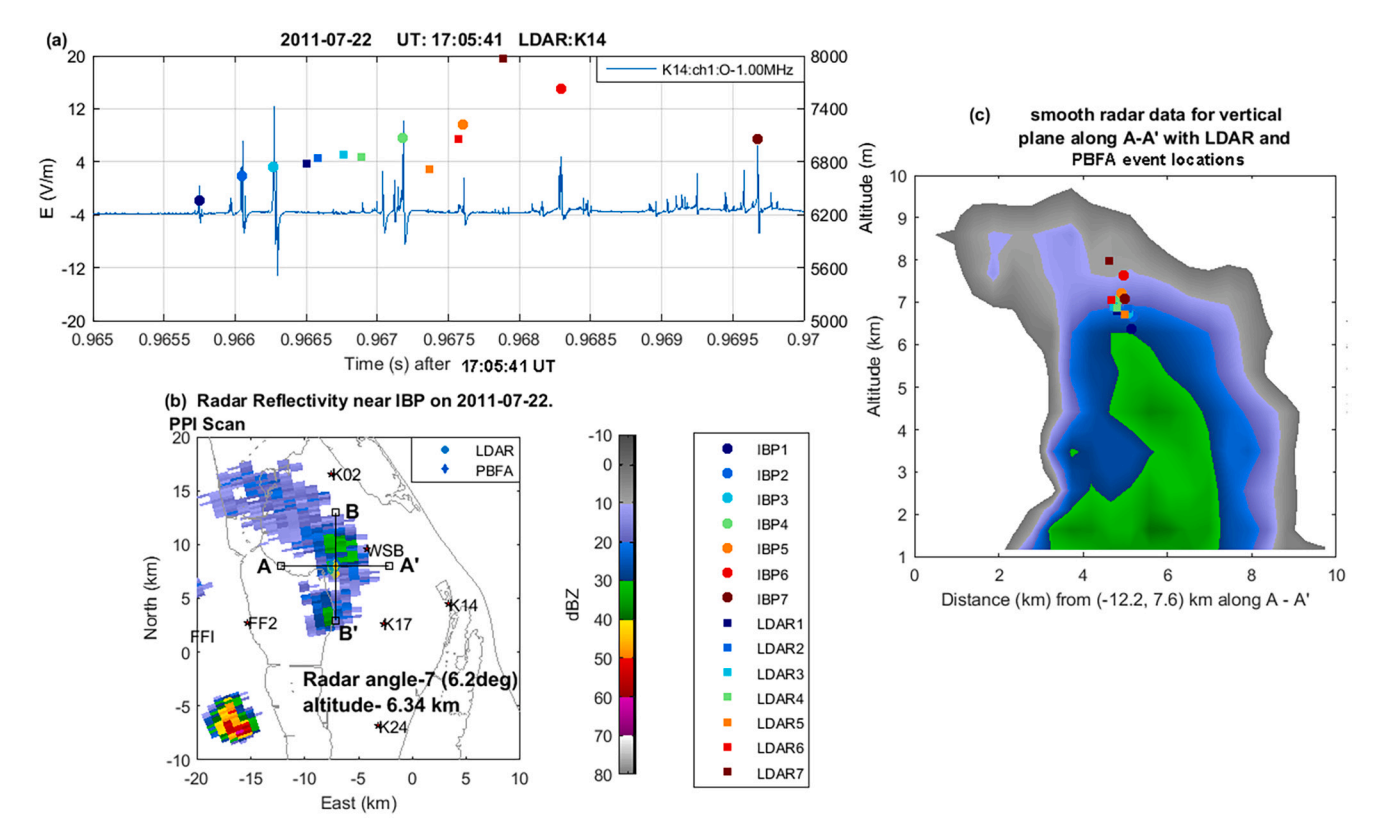


Fig. 8. As in Fig. 1, except showing data for Example 3, 22 July 2011, 1705:41 UT. (a) First 5 ms of Echange data and altitudes of modeled IBPs (IBP1–7) and LDAR sources vs time. (b) PPI of reflectivity, from KMLB radar, at scan angle that is near altitude of IBPs in the storm. Cross-section location A-A' through sources is shown. (c) West-to-east cross-section (along A-A') of reflectivity with PBFA and LDAR locations projected.

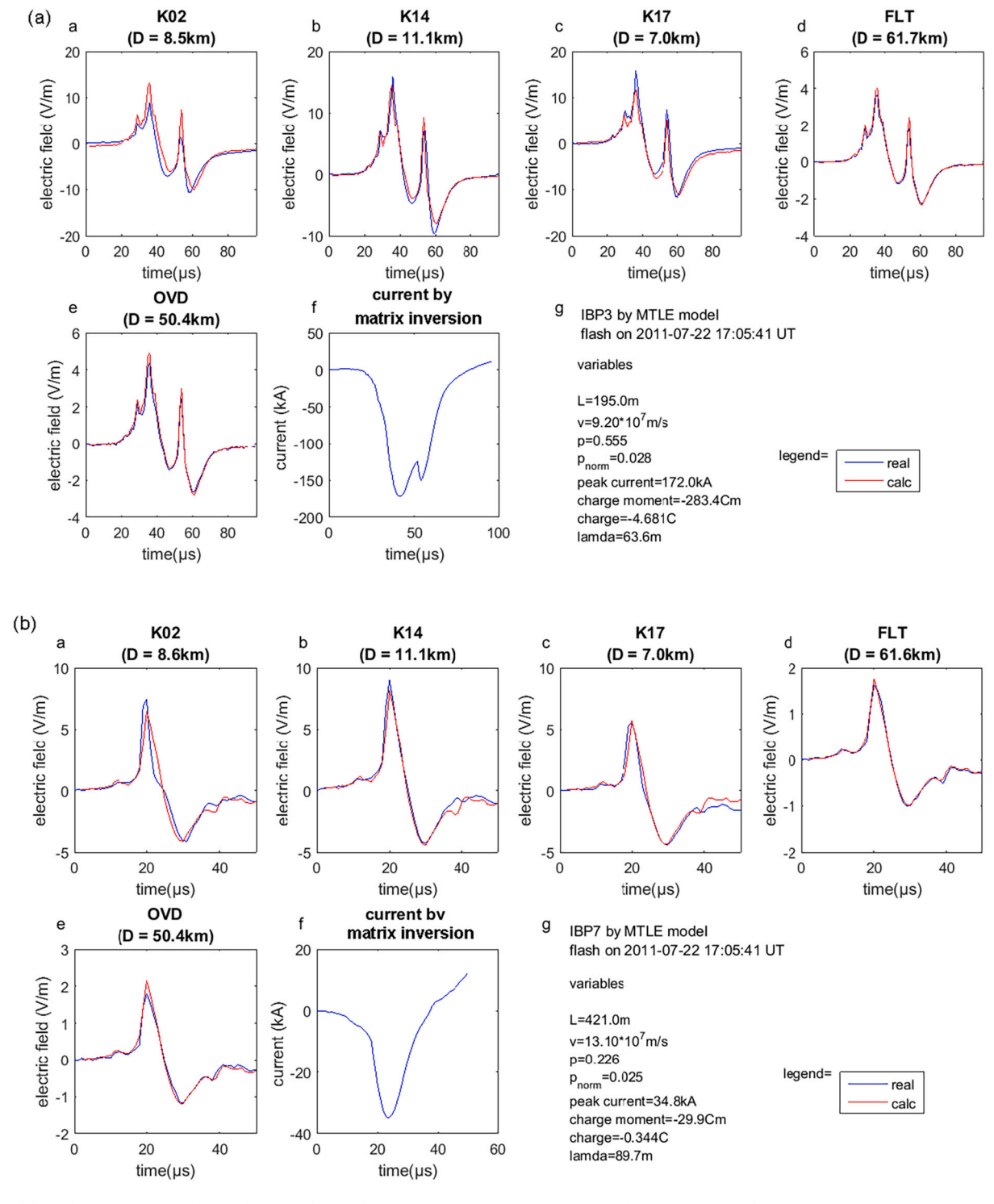


Fig. 9. Model results for two IBPs of Example 3, in which only two of five sensors are in the far-field region (D > 20 km). (a) As in Fig. 2a, except for IBP3 of the Example 3 flash. (b) As in Fig. 2a, except for IBP7 of Example 3. Both these IBPs are small in E-change amplitude and short in duration, although the peak current values are not small.

As in Examples 1 and 2, each successive IBP conducting channel length resulting from the model was close to the new vertical extension of the IBP (from the previous IBP), as determined from the PBFA locations. Unlike in Examples 1 and 2, this flash has no abrupt change in altitude of the pulses or in the modeled channel length and no extraordinary IBPs.

4.4. Example 4: 22 July 2011 at 1712:20 UT flash

The Example 4 flash occurred on 22 July 2011 at 1712:20 UT, at a distance of 6.8 km from the closest sensor (K02). This flash was in the same storm as, but nearly 5 min later than, Example 3. The PBFA and LDAR locations (not shown) indicated that the IB stage of this flash extended upward from 5.8 km to 6.8 km, where radar reflectivity ranged from about 28 dBZ to 10 dBZ. Five IBPs from the first 2 ms were modeled

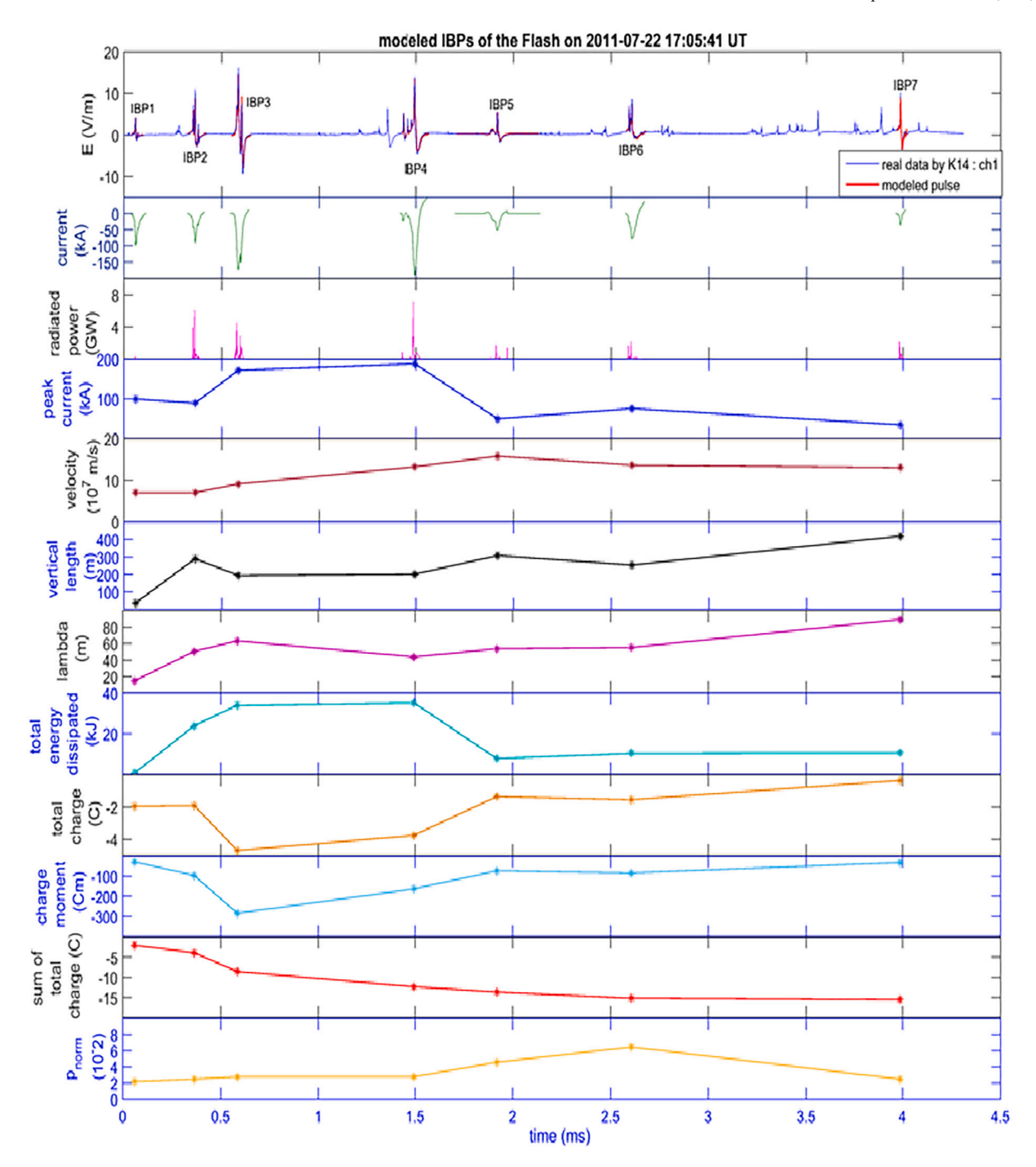


Fig. 10. As in Fig. 4, but showing results for seven modeled IBPs occurring through first 5 ms of Example 3 flash, 22 July 2011 at 1705:41 UT. Data in the top panel are from K14 site, compared to E-change pulses from the modeling method.

in this case, distributed as follows: classic IBP1, single subpulse classic IBP2, single subpulse classic IBP3, two subpulse classic IBP4, and two subpulse classic IBP5. There were no WWLLN events detected with this flash.

Obtained parameters of each modeled IBP of Example 4 are shown in Fig. 11 and listed in Table 4Fig. 11. Table 4 also includes minimum, maximum, average and standard deviation of each parameter. In terms of E-change amplitude, the modeled pulses were more uniform than in the other Examples; IBP2 and IBP3 were smallest (0.4 V/m), and IBP4 and IBP5 were largest (0.8 V/m). IBP1 had the minimum channel length (27 m) and total energy dissipated (0.8 kJ), and gave the largest peak current (111.9 kA), although IBP2 and IBP4 had similar peak current

values. IBP2 had the slowest velocity $(13\times10^7 \text{ m/s})$, and the range of velocities was up to $18\times10^7 \text{ m/s}$ in this series of results. IBP2 and IBP3 had the smallest total charge (0.3C), while IBP3 had the smallest peak current (11 kA). The maximum charge moment (102.7C m, IBP4) was rather small in this case, similar to the average value in Example 3. IBP5 had the maximum velocity $(18\times10^7 \text{ m/s})$, peak radiated power (5.4 GW) and total energy dissipated (32.7 kJ), with channel length of 350 m.

As in the earlier examples, each successive IBP conducting channel length from the model was approximately the same as the vertical extension of the IBP as determined from the PBFA locations. Like Example 3, the modeled part of this IB stage did not show any extraordinary pulses of the sort seen in Examples 1 and 2, nor was there

Table 3Obtained electrical and physical properties of Example 3 IBPs.

IBP number	Rise time (µs)	Fall time (µs)	Peak E at 100 km (V/ m)	Vertical length (m)	Velocity (10 ⁷ m/s)	Lambda (m)	Peak current (kA)	ρ norm (10 ⁻²)	Charge moment (C m)	Total charge (C)	Peak radiated power (GW)	Total energy dissipated (kJ)
1	11	36	0.5	38	7.1	14.9	99.8	2.2	-26.6	-1.93	0.3	0.6
2	18	30	1.1	291	7.1	50.6	89.6	2.5	-95.3	-1.89	6.1	24.0
3	12	35	1.9	195	9.2	63.6	172	2.8	-283.4	-4.68	4.5	34.1
4	64	28	1.7	202	13.3	43.9	189	2.8	-161.8	-3.74	7.2	35.3
5	31	29	0.7	310	15.9	53.9	50.0	4.6	-72.2	-1.34	1.8	7.8
6	16	34	0.9	255	13.7	55.4	76.1	6.5	-83.0	-1.53	2.2	10.4
7	10	14	1.1	421	13.1	89.7	34.8	2.5	-29.9	-0.34	2.2	10.6
min	10	14	0.5	38.0	7.1	14.9	34.8	2.2	-26.6	-0.34	0.3	0.6
max	64	36	1.9	421.0	15.9	89.7	189	6.5	-283.4	-4.68	7.2	35.3
avg	23	29	1.1	244.6	11.3	53.1	101.6	3.4	-107.5	-2.21	3.5	17.5
std	19	7	0.5	118.8	3.5	22.4	58.4	1.6	89.9	1.49	2.5	13.6

any abrupt and large change in altitude of the IBPs. Fig. 12 shows comparisons of various IBP parameters among the four IC flashes.

5. Possible mechanism of IBPs, EIPs, and TGF gamma-ray production

Kostinskiy et al. (2020) proposed a mechanism (called the KMS Mechanism herein) to explain lightning initiation and the first few IBPs of the IB stage of lightning flashes. In this section we outline the KMS Mechanism and then compare it to our model results for IBPs of IC flashes. The outline is based in part on a synopsis of the KMS mechanism in Stolzenburg et al. (2021).

In the KMS Mechanism flash initiation is caused by the almost simultaneous production of a very large number of positive streamer flashes. Each positive streamer flash begins in a small volume (3–60 cm³) called an E_{th} -volume with an electric field \geq 3 MV/(m·atm), the breakdown electric field. The many Eth-volumes needed are produced by turbulent motion of charged cloud and precipitation particles. Each streamer flash also requires a free electron to start the first positive streamer; the KMS Mechanism proposes that a free electron for each Ethvolume is provided by an extensive air shower (EAS) of a high energy cosmic ray (10¹⁵–10¹⁷ eV) that triggers a relativistic runaway electron avalanche (RREA). The proposed requisite turbulence is more likely in and around thunderstorm updrafts and downdrafts, especially at the interface between those regions of opposing vertical air motions (e.g., Brothers et al., 2018). For IC flashes the necessary Eth-volumes would be distributed in the thundercloud between the (lower) main negative charge region and the (upper) main positive charge region.

The KMS Mechanism describes IBPs as developing from the positive streamer flashes of flash initiation in a four stage process; Fig. 13 shows drawings of some of the key ideas. In the first stage, most of the positive streamer flashes transition to UPFs (Unusual Plasma Formations), which are hot channels with lengths of 1-30 cm (Kostinskiy et al., 2015a, 2015b). In the second stage, thousands of UPFs merge into bigger and bigger three-dimensional (3-D) UPF networks that consist of many short conducting channels connected in a complicated grouping of series and parallel channels that together have overall linear scales growing from 1 m to 100 m or more, while the total combined lengths of the series and parallel channels can range from 300 m to 3000 m or more. In Fig. 13b and c a developing 3-D UPF network is marked with "3." When two UPF networks merge, one with a length scale of ~50 m and one with a much shorter length, the merger will be seen with the E-change sensor as a narrow or intermediate IBP; these are called "preparatory mergers" in the KMS Mechanism. In the third stage, two 3-D networks, each with a scale ≥100 m, merge, and the merger will be seen with the E-change sensor as the first classic IBP. The merging process is shown schematically in Fig. 13a with the two merging UPF networks labeled "1" and "2." The merging includes a "breakthrough phase" and a "return stroke phase" that are shown in Fig. 13 and described in more detail below. If, during the third stage, a smaller UPF network connects to either of the

100 m scale UPF networks ("1" or "2" in Fig. 13a) just before they connect to make the classic IBP, the small or intermediate merger will be seen as a subpulse on the rising side of the classic IBP. It is also possible (and perhaps likely) that the breakthrough itself would cause a subpulse that would be seen near the beginning of the IBP, as discussed later. In the KMS Mechanism, the estimated lengths of conducting UPF channels in a classic IBP were roughly 500 m for a weaker classic IBP (charge of 0.2C) and 2500 m for larger amplitude classic IBPs (charge of 1.0C); the charge for the IBP current is stored in the corona sheaths of the conducting channels of the UPF networks. In the fourth stage, the KMS Mechanism proposes that after the first classic IBP, a new 3-D UPF network will develop above the two merged UPF networks; such development will involve new narrow and/or intermediate IBPs merging and growing into a large 3-D UPF network ("3" in Fig. 13b). The second classic IBP (possibly including subpulses) occurs when the third large 3-D UPF network merges with the previously merged 3-D UPF networks ("4" and "10" in Fig. 13c and d). The fourth stage is repeated for each subsequent classic IBP, with another 3-D UPF network merging with the larger and larger UPF network that consists of the previously merged networks. The first classic IBP is the beginning of the "initial leader" of the IC flash; the initial leader grows upward with the addition of each new large, 3-D UPF network (which causes each new classic IBP).

In Examples 1 and 2 we mentioned an "alternative hypothesis" for the relatively long time between the two extraordinary IBPs in each example, namely that in each example the IC flash may have "restarted" after the first extraordinary IBP. One way to restart a flash and get a second extraordinary IBP might be to have another extensive air shower interact with a turbulent region with many E_{th} -volumes, located 1–3 km above the first extraordinary IBP. The EAS/RREA process would then start UPFs which would combine into UPF networks, and the extending initial leader moving up from below would eventually (in 1–3 ms) merge with a large 3-D UPF network (caused by the new EAS/RREA) to make the second extraordinary IBP. This scenario might also help explain why the second extraordinary IBP in both Examples 1 and 2 appears as a group of three or four classic IBPs separated from each other by $<150~\mu s$. For this scenario, two extensive air showers would need to occur in almost the same location separated by <10 ms, but this is not impossible, rather it is quite unlikely, just as it is quite unlikely to have three or four IBPs that are also EIPs in the same IC flash (as in Examples 1 and 2).

One of the main questions about IBPs in IC flashes that is approachable using the modeling results herein and the KMS Mechanism is What causes the subpulses before (and occasionally after) the main peak of a classic IBP? Subpulses of a classic IBP are likely smaller UPF networks connecting to one of the two large 3-D UPF networks that combine to make the main peak of the classic IBP (i.e., both smaller and larger UPF networks are merging). One subpulse might be caused by the "breakthrough phase" during the merger. Hence, we conclude that in a classic IBP with multiple subpulses, the IBP current is due to the sum of individual subpulse currents adding to the main peak current (caused by the "return stroke phase" of the two merging large UPF networks). See

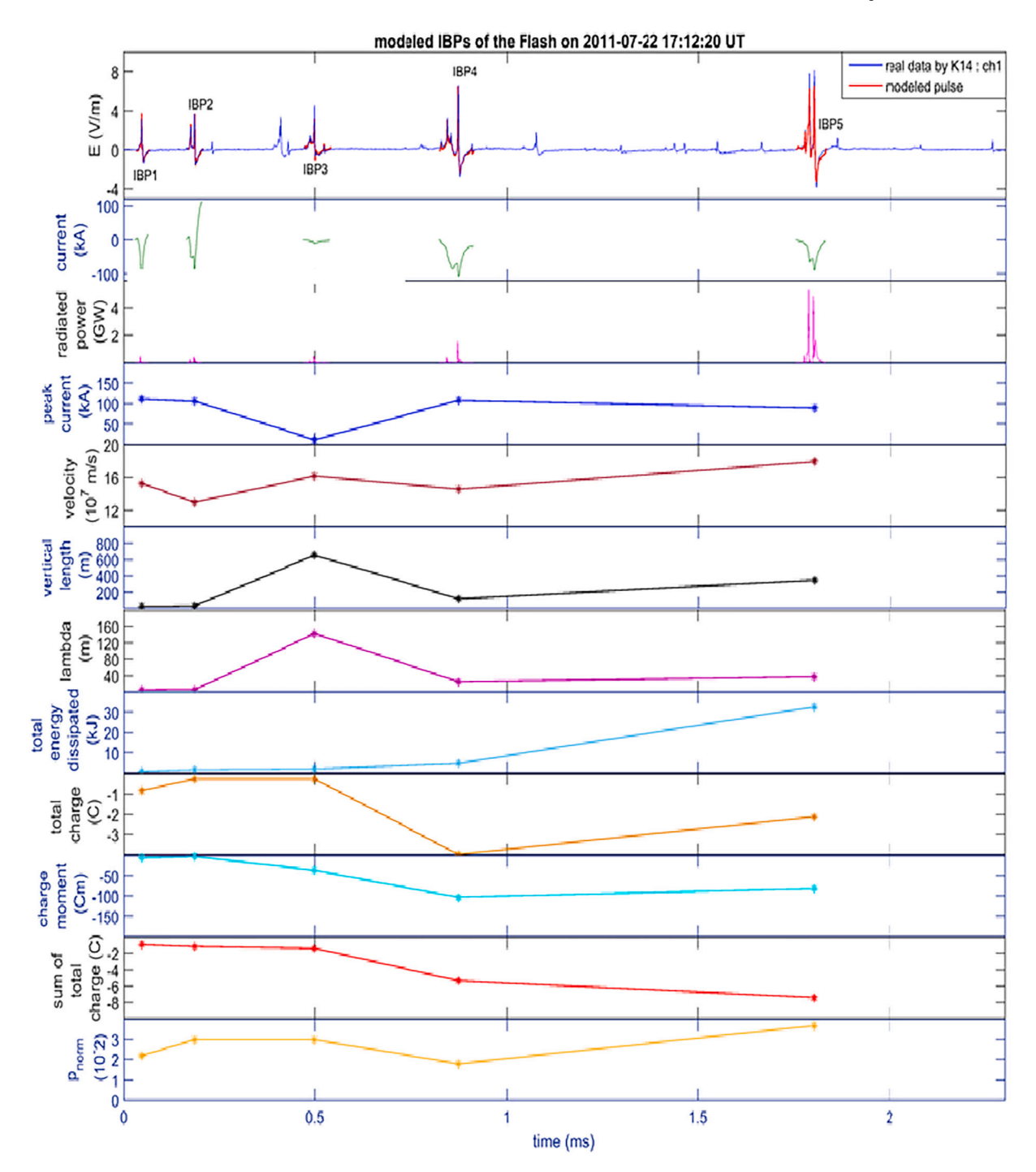


Fig. 11. As in Fig. 4, but showing results for five modeled IBPs occurring through the first 2 ms of Example 4 flash, 22 July 2011 at 1712:20 UT. Data in the top panel are from K14 site, compared to E-change pulses from the modeling method.

Fig. 2b for an example of small currents causing subpluses.

Physically, using these modeling results and the KMS Mechanism, we can also address another question: If a classic IBP with a peak current > 150~kA is an EIP and therefore the radio signal of a TGF, what causes the gamma-rays? Although the KMS Mechanism does not discuss TGFs, it does describe the powerful light and electromagnetic radiation emitted when two 3-D UPF networks connect to make a classic IBP. Also, in the KMS Mechanism the charge moved by the IBP current is stored on the corona sheaths of the conducting channels of the UPF network that is connecting to the initial leader, so in general a larger current requires a larger stored charge and therefore a larger 3-D UPF network. Cummer et al. (2015) have shown that TGFs occur several milliseconds after IC

flash initiation, when the initial leader is 1–2 km in length; i.e. after a few classic IBPs have already occurred. We hypothesize that TGFs are produced during the "breakthrough phase" of a classic IBP, which we now describe. Fig. 13a and b show that the first classic IBP involves the merging of two large UPF networks. One UPF network sends a positive leader toward the other UPF network, which simultaneously sends a negative leader toward the first UPF network. The "breakthrough phase" (marked with "4" in Fig. 13a) occurs when these two leaders meet, forming a "common streamer zone" ("4" in Fig. 13a is supposed to represent the common streamer zone); almost immediately the two leaders connect and a large current (the "return stroke," marked with "10" in Fig. 13b) flows between the two UPF networks (e.g., Kostinskiy

Table 4Obtained electrical and physical properties of Example 4 IBPs.

IBP number	Rise time (µs)	Fall time (µs)	Peak E at 100 km (V/ m)	Vertical length (m)	Velocity (10 ⁷ m/s)	Lambda (m)	Peak current (kA)	ρ norm (10 ⁻²)	Charge moment (C m)	Total charge (C)	Peak radiated power (GW)	Total energy dissipated (kJ)
1	5	12	0.5	27	15.3	5.9	112	2.2	-4.8	-0.83	0.5	0.8
2	12	6	0.4	33	13.0	6.5	107	3.0	-1.6	-0.25	0.4	1.6
3	15	42	0.4	658	16.2	143.0	11.0	3.0	-36.0	-0.25	0.5	2.0
4	40	41	0.8	120	14.6	26.1	109	1.8	-102.7	-3.97	1.6	4.9
5	25	24	0.8	350	18.0	38.0	89.4	3.7	-80.6	-2.11	5.4	32.7
min	5	6	0.4	27	13.0	5.9	11.0	1.8	-1.6	-0.3	0.4	0.8
max	40	42	0.8	658	18.0	143.0	112	3.7	-102.7	-4.0	5.4	32.7
avg	19.4	25.0	0.6	237.6	15.4	43.9	85.6	2.7	-45.1	-1.5	1.7	8.4
std	13.6	16.4	0.2	269.0	1.9	57.0	42.6	0.7	45.2	1.6	2.1	13.7

et al., 2016). Since substantial electric fields must develop between the connecting, oppositely charged leaders in the common streamer zone, we hypothesize that these electric fields might be sufficient to produce the gamma-rays of a TGF. As mentioned above, the breakthrough current might cause a subpulse at the beginning of the IBP. Then, after the leaders connect, the "return stroke" current flowing for hundreds of meters between and through the connecting UPFs makes the classic IB pulse detected by the E-change sensors. The second classic IBP and subsequent classic IBPs occur in a similar way, as shown in Fig. 13c and d, when another large UPF network merges with first connected pair of UPF networks (the nascent initial leader). For an IBP to be an EIP (with current >150 kA), it may be that the charge of the UPF network connecting to the initial leader needs to be especially large to make the large EIP current as well as the large electric field to make MeV gamma-rays. If this is the correct mechanism for making IBPs, then one might expect gamma-rays of differing peak energies depending on the magnitudes of the charges on the connecting 3-D UPF networks. In particular, for an IBP to cause a detectable TGF at a satellite, we would expect that an especially large UPF network would have to connect to the initial leader.

6. Extraordinary IBPs and TGFs

As discussed above, in IC flash Example 1 there were three extraordinary IBPs (IBP6, IBP9c, and IBP9d) that each had the characteristics of an EIP, which are the radio signal of a TGF event (Lyu et al., 2016). Hence, we might expect as many as three TGFs from this IC flash, with the first TGF (from IBP6) occurring 4 ms before the last two TGFs, and the last two TGFs separated by about 120 µs (time between peaks of IBP9c and IBP9d). There are already examples of multiple-TGF events in the literature. In their ground-breaking discovery of TGFs, Fishman et al. (1994) reported on twelve TGFs and noted that four of them were double-peak TGFs with peak separations of 1-4 ms. Fishman et al. (2011) reported three pairs of TGFs (labeled #6, #12, #26) in data from the Gamma-Ray Burst Monitor on the Fermi Observatory; the two TGFs in the pairs were separated in time by 1.3, 8.4, and 1.4 ms, respectively. Fishman et al. (2011) called the pairs "double-pulse TGF events" and stated that their cause was "unknown." Fishman et al. (2011) also highlighted three TGF events (#11, #12b, and #13) in which two TGF pulses were "partially overlapping"; the overlapping TGFs were separated by 300-450 µs (see also Briggs et al., 2010). Mezentsev et al. (2016) have reported on double-pulse and overlapping TGFs detected by the RHESSI satellite; some of these TGFs had coincident WWLLN events.

As described, event #12 in Fishman et al. (2011) was a double-pulse TGF event with the TGFs separated by 8.4 ms, and the second TGF (#12b) consisted of two partially overlapping TGFs separated by 300 μ s, for a total of three TGFs. The sequence of EIPs in our IC flash Example 1 is quite similar to those in TGF event #12 in Fishman et al. (2011), with the first two events separated by 4 ms and the last two separated by 120 μ s. In the series of developing IBPs in IC flash Example 1, the three largest IBPs were EIPs and presumably caused TGFs.

Using similar reasoning, we might expect there were as many as four

TGFs in IC flash Example 2, from the extraordinary IBPs (IBP7, IBP8a, IBP8b, and IBP8c), since these events also had the characteristics of EIPs. IBP7 occurred 3.2 ms before IBP8a, making them a possible "double-pulse TGF event" as defined by Fishman et al. (2011). The three possible TGFs of IBP8a, IBP8b, and IBP8c would probably have been overlapping with the successive pairs of TGFs separated by 140 and 60 μs.

A final note about Energetic IC Pulses: our model results allow us to give values for the total energies of the EIPs in our data. In Example 1, the first EIP (IBP6) had an energy of 790 kJ, while the energy of IBP9 (which included two EIPs) was 490 kJ. In Example 2, the first EIP (IBP7) had an energy of 1400 kJ, while the energy of IBP8 (which included three EIPs) was 2600 kJ. These results suggest that our EIPs dissipate energies in the range of 250–2000 kJ. For comparison, excluding the EIPs from Tables 1–4, the other 25 IBP energies had ranges of 1–135 kJ, 0.4–7 kJ, 0.6–35 kJ, and 0.8–33 kJ in Examples 1–4, respectively. These results indicate that the seven modeled IBPs characterized as EIPs are indeed very energetic.

7. Discussion

Fig. 12 summarizes several properties of the 29 modeled IBPs. Vertical channel lengths are mostly in the 100-650 m range, with four lengths <100 m, while the four extraordinary IBPs had lengths >750 m long. Current velocities are mostly in the range of $10-16.9 \times 10^7$ m/s, with five values slower than 10×10^7 m/s and five values of $17-21 \times 10^7$ m/s (including three extraordinary IBPs). Generally, Fig. 12a indicates range normalized E-change amplitude and current velocity both tend to increase with increasing channel length, although the correlations are quite weak if the extraordinary pulses are excluded. In Fig. 12b the total charge moved by 21 IBPs is less than 3C, with four IBPs moving 3-5C, while the extraordinary pulses moved 8-72C due to their longer current durations and larger peak currents. Similarly, most of the charge moment values are <100C m, a few others are in the 100-300C m range, while the four extraordinary IBPs had extraordinary magnitudes of 3450-20,050C m. Overall, Fig. 12b indicates the total charge and charge moment tend to increase with increasing channel length when the longest lengths are included, but there is almost no relation between these properties among the typical pulses (i.e., excluding the extraordinary IBPs). This finding of essentially random variation of IBP parameters through the early part of the IB stage fits reasonably well with the KMS Mechanism, since each UPF network may have differing amounts of charge when it connects to the initial leader to cause the next IBP.

Fig. 12c compares IBP peak current and IBP total charge moved to IBP E-change amplitude range normalized to 100 km, and in general current and charge tend increase similarly with increasing E-change amplitude. Since few well-documented values of peak currents of IC IBPs exist, it is noteworthy that the 29 IBP peak currents are so large, even for early IBPs: 17 of the values are in the range 20–150 kA, only six are <20 kA, and six are >150 kA (the EIP threshold), including the currents of the four extraordinary IBPs, 217–359 kA (Fig. 12c). (Recall that IBP9 of

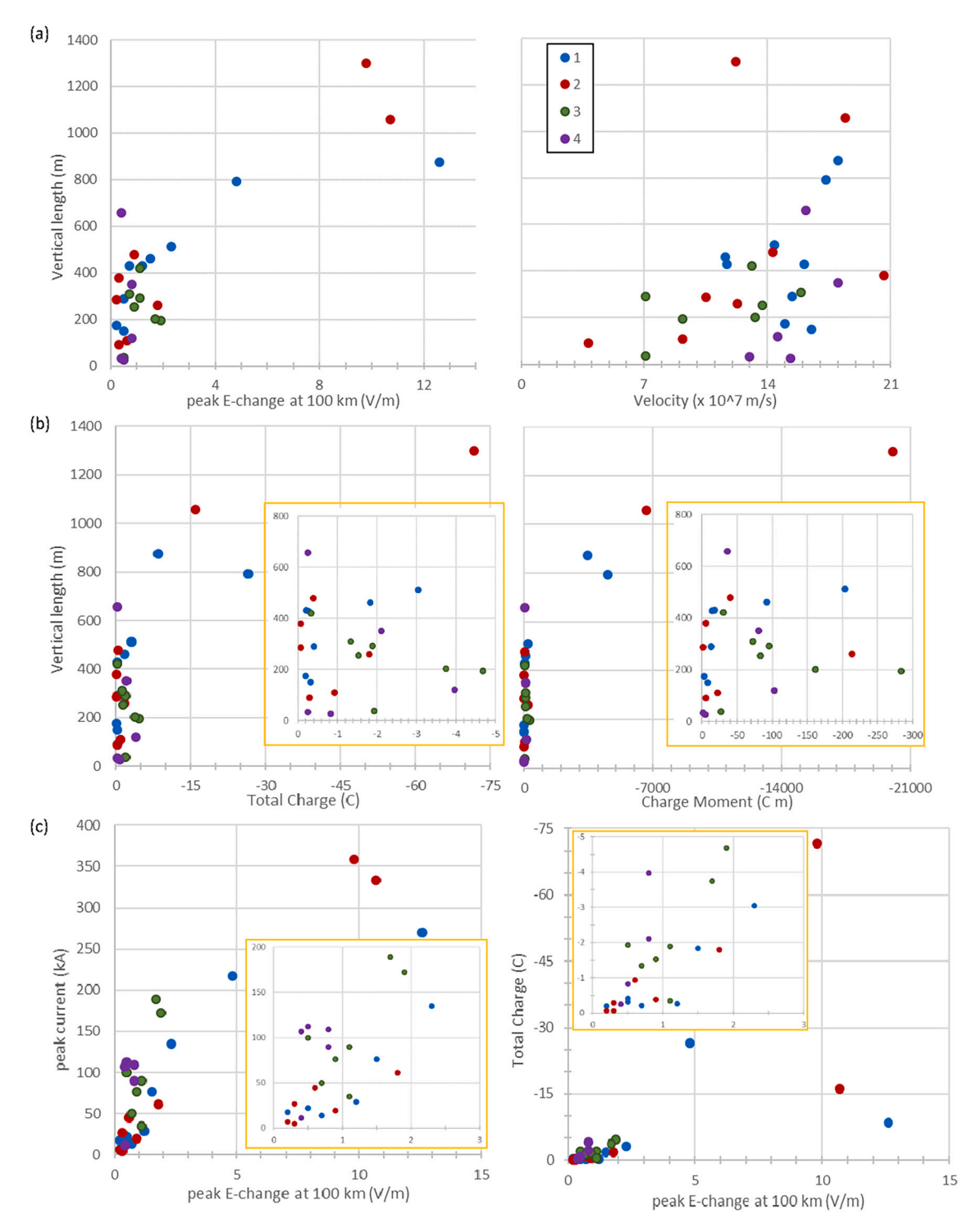


Fig. 12. Summary of model results for 29 IBPs from four IC flashes, Examples 1–4. (a) Variation of rangenormalized E-change amplitude and velocity with channel length. (b) Variation of total charge and charge moment with channel length. (c) Variation of peak range-normalized E-change amplitude with peak current and total charge. Insets in (b) and (c) are expanded views of lower left corner, with 25 of the 29 IBPs. In all the plots, the four IBPs considered 'extraordinary' pulses (IBPs 6 and 9 in Example 1, and IBPs 7 and 8 in Example 2) are extreme values.

Example 1 and IBP8 of Example 2 were interpreted as groups of four and three classic IBPs, respectively, so there were in total 34 IBPs with modeled currents, and 11 IBPs had peak currents >150 kA.) The large peak currents of extraordinary IBPs help explain why they are sometimes detected by WWLLN. The four extraordinary IBPs are also associated with large radiated power (35–185 GW) and large dissipated energy (487–2675 kJ), while the other 25 IC IBPs give powers <22 GW (most are <5 GW) and energies <136 kJ (most are <13 kJ).

One of the main findings in Karunarathne et al. (2020) about IBPs of CG flashes was that for each flash the first or second IBP of the IBP series had the largest peak current with values of 19, 24, 127 kA. In contrast, for the four IC flashes studied herein the largest peak current often occurred later in the series with values of 270, 359, 172, 112 kA for IBP6, IBP8, IBP3, and IBP1, respectively. Also, in the CG flashes the IBP current velocity was smallest for the first classic IBP and increased "mostly monotonically" during each series of classic IBPs, while in the IC

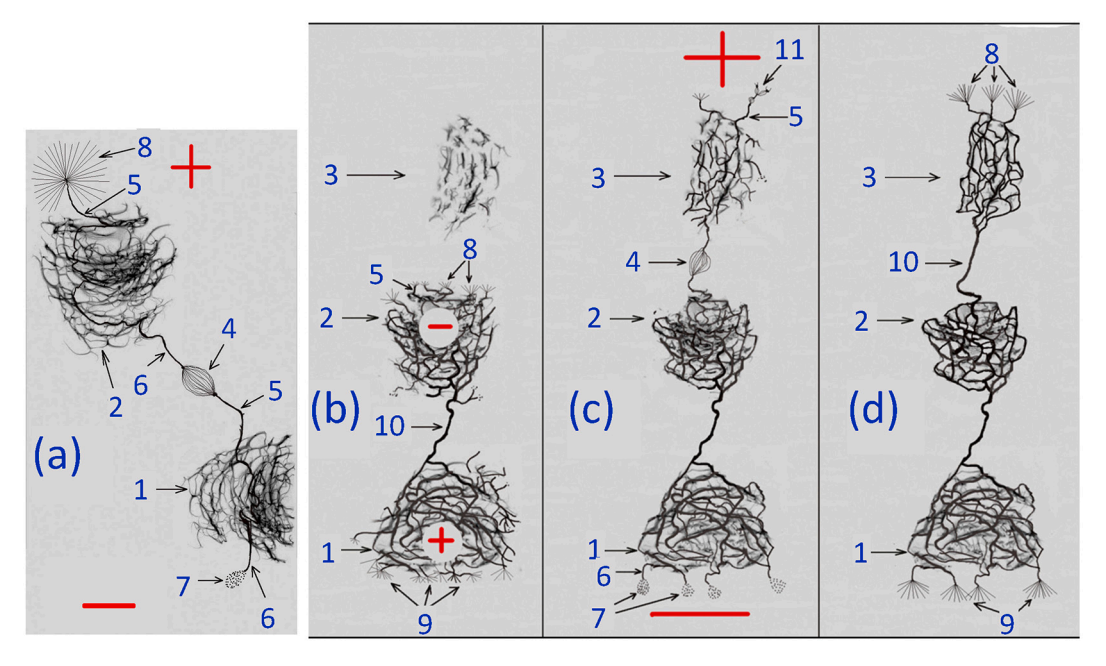


Fig. 13. Sketch of development of classic IBPs in IC flashes, adapted from Fig. 10 of Kostinskiy et al. (2020). The cloud charges driving the development are indicated by the red plus and minus signs in (a) and (c) and are the same (but not shown) in (b) and (d). (a) For IBP1, the moment of connection (marked with "4") between the upward-moving negative leader (of UPF network #1) and downward-moving positive leader (from UPF network #2) is depicted. This is the "breakthrough" phase of IBP1. (b) The "return stroke" phase of IBP1 (marked with "10") is shown. The plus and minus signs inside "1" and "2" are the polarities of charges induced on the merged UPFs by the cloud electric field. Note that the electric fields of the induced charges and the cloud charges help cause the development of UPF #3. (c) For IBP2, the moment of connection (marked with "4") between plasma networks #2 and #3 is depicted. (d) "Return stroke" phase of IBP2 is shown. Numbered objects: 1 - first 3-D UPF network, 2 - second 3-D UPF network, 3 - third 3-D UPF network, 4 - breakthrough phase of contact between plasma networks, 5 - negative leader, 6 - positive leader, 7 - streamer crown of positive leader, 8 - flash of streamer crown of negative leader, 9 - flash of streamer crown of positive leader, 10 - plasma channel of the "return stroke" phase of contact between plasma networks, 11-streamer crown of negative leader. (For interpretation of the references to color in this figure legend, the reader is referred to the web version of this article.)

flashes studied herein, the distribution of IBP current velocities varies with no obvious trend. These comparisons provide additional support for the notion that the development of classic IBPs in IC flashes is quite different from the development of classic IBPs in CG flashes.

Tables 1 and 2 (for IC flash Examples 1 and 2) include the minimum, maximum, average, and standard deviation of each IBP characteristic in two ways: using all IBPs and using all except the extraordinary IBPs. Comparing the averages with and without the extraordinary IBPs shows how strongly the extraordinary IBPs affect the averages. Note also that the averages in Tables 1 and 2 without extraordinary IBPs are in reasonable agreement with aveages in Tables 3 and 4 for IC flash for Examples 3 and 4, which did not have any extraordinary IBPs.

To further underscore the magnitude of the four extraordinary IBPs, we note that their range-normalized E-change amplitudes were 4.8, 9.8, 10.7, and 12.6 V/m at 100 km. These values are extraordinary compared to Smith et al. (2018), who studied the largest IBP in 40 IC flashes (in this same region of Florida) and found that the mean E-change amplitude (of the largest IBP) was 1.49 V/m, with only 2 of 40 values exceeding 4.0 V/m (4.3 and 8.4 V/m). Stolzenburg et al. (2016) investigated luminosity coincident with "large amplitude" IC IBPs during four hybrid flashes, but the largest IC-type IBPs in their study had range normalized *E*-change amplitudes of 2.2–3.4 V/m, hence smaller than the extraordinary IBPs in this study.

Previous high-speed video studies have indicated that the length of the conductive channel increases through the IB stage of CG flashes (Stolzenburg et al., 2013, 2014, 2020). However, there are no video observations of channel length in the IB stage of IC flashes to provide evidence for this tendency. In this study, the model results indicate that channel length through which the IBP current travels does generally increase with successive IBPs (see Figs. 4, 7, 10, and 11). Together, PBFA locations and model-derived channel lengths indicate that most of these IBPs extend the conductive channel upward through the IB stage: for

each successive IBP the length of the current-carrying channel is similar to the vertical extension of the IBP from the previous one, as determined from their PBFA locations.

We have been able to understand, at least partially, the physical mechanisms behind two features of IC IBPs: multiple subpulses and differing risetime/falltime ratios. Figs. 2b and 6a show details of the current behavior of two IBPs with multiple subpulses. These figures show that IBPs with multiple subpulses on the main positive pulse have noticeable 'humps' or sudden increases in the derived current that are coincident with each subpulse. We conclude that subpulses appear to be due to small, individual current impulses, each adding to the main current of the IBP. As shown in the four Tables, we also found that 23 of 29 IBPs have a longer falltime than risetime, while four IBPs have significantly longer risetimes than falltimes, namely, IBP6 in Ex.1, IBP7 in Ex.2, and IBPs 4 and 5 in Ex.3 (see Fig. 2b for a detailed look at the rise and fall times of IBP6 in Ex.1). These four IBPs all had 3-4 subpulses on the rising side of the classic IBP, and we conclude that currents associated with multiple subpulses can cause the overall IBP risetime to be longer than its falltime. (Note that although IBP9 in Ex.1 and IBP8 in Ex.2 are listed with longer risetimes than falltimes, they were excluded from this discussion because they are also interpreted as having multiple classic IBPs too close together to find individual risetimes and falltimes.) Note that the KMS Mechanism readily accounts for multiple subpulses: they are smaller UPF networks connecting to one or the other of the two large UPF networks either just before or just after these two large networks merge to make the classic IBP. The KMS Mechanism also is consistent with the first subpulse of an IBP being caused by the breakthrough phase of the two large connecting UPF networks.

Another goal of this project has been to study the IC IB stage as a series. The observed and calculated properties of these 29 pulses allow us to describe typical values and thereby better identify atypical or extraordinary pulses of interest. Relationships among the parameters

provide information to understand the physical characteristics of the IC IB stage. In particular, the findings that peak range normalized *E*-change, peak current, total charge, charge moment, peak radiated power, and total energy dissipated increase with increasing channel length, and that peak range normalized E-change, peak radiated power, and total energy dissipated increase with increasing peak current together indicate that as the channel length generally increases through the IB stage, the pulses have greater effect on charge motion for further flash development. The apparently weak relation between current velocity and channel length provides (at best) only weak support for increasing conductivity along the initial leader path through the early part of the IC IB stage, in contrast to the findings from studying series of CG IBP with similar techniques (Karunarathne et al., 2020).

8. Conclusions

The initial breakdown (IB) stage of intracloud (IC) lightning flashes is among the most difficult and interesting of lightning events to study. The initial breakdown pulses (IBPs) occur in the middle of the cloud and are therefore difficult to observe directly, while their special features, such as numerous (3–5) subpulses superimposed on the main bipolar pulse and satellite-detected gamma ray emissions, are usually not found with other discharges. This study is the first to determine IBP currents in IC flashes via modeling; we modeled a series of IBPs in the first 2-7 ms of four IC flashes using data from a ten-station calibrated electric field change (E-change) antenna array recorded in Florida in 2011. The IBP current waveforms were derived from the E-change data by the Matrix Inversion method; then an MTLE (Modified Transmission Line Exponentially decreasing) model determines the best channel length and current velocity to match the IBP data (Karunarathne et al., 2019). The current and derived properties of the IBPs, including peak current, total charge, charge moment, total energy dissipated, and radiated power, are described and listed for the four IC flashes in Tables 1-4. Flash Examples 1 and 2 herein each had two "extraordinary" IBPs with very large Echange amplitudes (4.8-12.6 V/m, range-normalized to 100 km) and very large peak currents. In contrast, the other 25 modeled IBPs in the four flashes were more typical and had relatively small E-change amplitudes, with most values in the range 0.2-1.2 V/m and five values between 1.3 and 2.4 V/m.

The main conclusions of this work are as follows:

- 1. The Matrix Inversion/MTLE modeling technique is able to fit the calibrated E-change data of IBPs of an IC flash at multiple sites remarkably well, even for complicated IBPs with multiple subpulses and long durations. As shown in Figs. 2, 3, 6, and 9, a single IBP current waveform with specified peak current can fit the E-change data at 5–7 sensor sites located at ranges of 7–101 km from the IBP, thereby providing confidence in the IBP currents and in the other derived IBP parameters.
- 2. The peak currents of classic IBPs of IC flashes are large, with 19 of 29 modeled IBP peak currents >30 kA, including 6 IBPs having peak currents >150 kA, and a maximum of 359 kA. The other ten IC IBPs had peak currents ≤30 kA. For comparison, in 25 CG IBPs modeled by Karunarathne et al. (2020), there was only one IBP with peak current >30 kA (with a value of 127 kA). Superimposed on the main pulse, the subpulses of classic IBPs appear to be due to small, individual currents, each adding to the main current of the IBP. Furthermore, if there are many subpulses on the rising side of the leading peak of the main bipolar pulse, then the overall current risetime of the classic IBP can be longer than its falltime.
- 3. For each successive classic IBP in the series of IBPs in IC flashes, the modeled IBP conducting channel length was close to the vertical extension length of the IBP from the prior IBP, as determined from their PBFA locations. This result is in keeping with the MTLE model used to represent the (exponentially decreasing, downward directed) current. The finding indicates that most of the IBP current is flowing

from the new IBP location only as far back (down) to the prior IBP location, with little remaining current traveling all the way back along the entire initial leader path to the flash initiation point. This model result for IC flash IB stages differs from what has been inferred from high-speed video data for CG flash IB stages (e.g., Stolzenburg et al., 2020).

- 4. The total energies dissipated by classic IBPs of IC flashes in the bandwidth 1.6–630 kHz are also large. Herein, IBP energy is found by integrating the IBP radiated power over the IBP duration (Eq. (6)), and the IBP radiated power (Eq. (5)) is proportional to the square of the time derivative of the IBP current. For the 29 IC IBPs modeled, there were 19 IBPs in the energy range 0.4–15 kJ, 6 IBPs in the range 15–450 kJ, and 4 IBPs in the range 450–2700 kJ. For comparison, all of the 25 CG IBPs modeled by Karunarathne et al. (2020) had energies <15 kJ. Also, we find that the modeled IC IBPs that are characterized as EIPs (Energetic In-cloud Pulses) have estimated energies in the range of 250–2000 kJ.
- 5. In two of the four IC flashes (Examples 1 and 2), the series of modeled IBPs included, respectively, three and four IBPs having the characteristics of EIPs, including current >150 kA and altitude in the range of 8–13 km. EIPs are described by Lyu et al. (2016) as "the radio signal" of a TGF event. In both IC flashes (Examples 1 and 2), there was a pair of IBP/EIP events separated by 3–4 ms that could have caused "double-pulse TGFs," as found and discussed in Fishman et al. (1994, 2011) and Mezentsev et al. (2016). In these flashes there were two or three IBP/EIPs separated by 60–140 μs that could have caused overlapping TGFs (Briggs et al., 2010; Fishman et al. 2011; Mezentsev et al., 2016). Thus a series of IBPs in IC flashes can explain double-pulse TGFs and overlapping TGFs, even in a single IC flash.
- 6. The data and modeling results for IC IBPs are consistent with the KMS Mechanism of flash initiation and IBP development (Kostinskiy et al., 2020). The KMS Mechanism can readily account for the wide range of IBP parameters found in IC flash Examples 1–4, since these parameters depend mainly on the charge stored on the corona sheaths of the large 3-D UPF (Unusual Plasma Formations) network that connects to the initial leader to make the IBP. As hypothesized by Kostinskiy et al. (2020), the IBP charge is also quite variable since it depends on the number of UPFs in the large 3-D UPF network, and these UPFs develop from the positive streamer flashes started by EAS/RREA electrons passing through many small regions with breakdown electric fields distributed along the initial leader path.

Declaration of Competing Interest

None.

Acknowledgements

The authors wish to thank the World Wide Lightning Location Network (http://wwlln.net), a collaboration among over 50 universities and institutions, for providing the WWLLN lightning location data used in this paper. We also thank Nadeeka Karunarathna for help with plotting radar data. This work was supported by US National Science Foundation grants AGS-1110030, AGS-1427734, and AGS-1745931, and it comprises a portion of the PhD dissertation research of the lead author.

References

Beasley, W.H., Uman, M.A., Rustan, P.L., 1982. Electric fields preceding cloud-to-ground lightning flashes. J. Geophys. Res. 87 (C7), 4883–4902.

Bils, J.R., Thomson, E.M., Uman, M.A., Mackerras, D., 1988. Electric field pulses in close lightning cloud flashes. J. Geophys. Res. 93, 15933–15940. https://doi.org/ 10.1029/JD093iD12p15933.

Briggs, M.S., et al., 2010. First results on terrestrial gamma ray flashes from the Fermi Gamma-ray Burst Monitor. J. Geophys. Res. 115, A07323 https://doi.org/10.1029/ 2009JA015242.

- Brothers, M.D., Bruning, E.C., Mansell, E.R., 2018. Investigating the relative contributions of charge deposition and turbulence in organizing charge within a thunderstorm. J. Atmos. Sci. 75, 3265–3284. https://doi.org/10.1175/JAS-D-18-0007.1
- Clarence, N.D., Malan, D.J., 1957. Preliminary discharge processes in lightning flashes to ground. Q. J. R. Meteorol. Soc. 83, 161–172.
- Coleman, L.M., Marshall, T.C., Stolzenburg, M., Hamlin, T., Krehbiel, P.R., Rison, W., Thomas, R.J., 2003. Effects of charge and electrostatic potential on lightning propagation. J. Geophys. Res. 108 (D9), 4298. https://doi.org/10.1029/ 2002/ID002718
- Connaughton, V., Briggs, M.S., Xiong, S., Dwyer, J.R., Hutchins, M.L., Grove, J.E., et al., 2013. Radio signals from electron beams in terrestrial gamma ray flashes. J. Geophys. Res. Space Physics 118, 2313–2320. https://doi.org/10.1029/ 2012JA018288.
- Cummer, S.A., Briggs, M.S., Dwyer, J.R., Xiong, S., Connaughton, V., Fishman, G.J., et al., 2014. The source altitude, electric current, and intrinsic brightness of terrestrial gamma ray flashes. Geophys. Res. Lett. 41, 8586–8593. https://doi.org/10.1002/2014GL062196.
- Cummer, S.A., Lyu, F., Briggs, M.S., Fitzpatrick, G., Roberts, O.J., Dwyer, J.R., 2015. Lightning leader altitude progression in terrestrial gamma-ray flashes. Geophys. Res. Lett. 42, 7792–7798. https://doi.org/10.1002/2015GL065228.
- Fishman, G.J., et al., 1994. Discovery of intense gamma-ray flashes of atmospheric origin. Science 264, 1313–1316.
- Fishman, G.J., et al., 2011. Temporal properties of the terrestrial gamma-ray flashes from the Gamma-Ray Burst Monitor on the Fermi Observatory. J. Geophys. Res. 116, A07304 https://doi.org/10.1029/2010JA016084.
- Gurevich, A.V., Zybin, K.P., 2005. Runaway breakdown and the mysteries of lightning. Phys. Today 58, 37–43.
- Hutchins, M.L., Holzworth, R.H., Rodger, C.J., Brundell, J.B., 2012. Far field power of lightning strokes as measured by the World Wide Lightning Location Network, JTech. J. Atmos. Ocean. Technol. 29 (8), 1102–1110. https://doi.org/10.1175/ JTECH-D-11-00174.1.
- Karunarathna, N., Marshall, T.C., Stolzenburg, M., Karunarathne, S., 2015. Narrow bipolar pulse locations compared to thunderstorm radar echo structure. J. Geophys. Res. Atmos. 120 (22), 11690–11706. https://doi.org/10.1002/2015JD023829.
- Karunarathna, N., Marshall, T.C., Karunarathne, S., Stolzenburg, M., 2017. Initiation locations of lightning flashes relative to radar reflectivity in four small Florida thunderstorms. J. Geophys. Res. Atmos. 122 (12), 6565–6591. https://doi.org/ 10.1002/2017JD026566.
- Karunarathne, S., Marshall, T.C., Stolzenburg, M., Karunarathna, N., Vickers, L.E., Warner, T.A., Orville, R.E., 2013. Locating initial breakdown pulses using electric field change network. J. Geophys. Res. Atmos. 118 (13), 7129–7141. https://doi. org/10.1002/jgrd.50441.
- Karunarathne, S., Marshall, T.C., Stolzenburg, M., Karunarathna, N., 2014. Modeling initial breakdown pulses of CG lightning flashes. J. Geophys. Res. 119 (14), 9003–9019. https://doi.org/10.1002/2014JD021553.
- Karunarathne, N., Karunarathne, S., Marshall, T.C., Stolzenburg, M., 2019. Modeling initial breakdown pulses of lightning flashes using a matrix inversion method. Radio Sci. 54 (3), 268–280. https://doi.org/10.1029/2018RS006695.
- Karunarathne, N., Marshall, T.C., Karunarathne, S., Stolzenburg, M., 2020. Studying sequences of initial breakdown pulses in cloud-to-ground lightning flashes.
 J. Geophys. Res. Atmos. 125 https://doi.org/10.1029/2019JD032104
 e2019JD032104
- Kitagawa, N., Brook, M., 1960. A comparison of intracloud and cloud-to-ground lightning discharges. J. Geophys. Res. 65 (4), 1189–1201.
- Koshak, W.J., Krider, E.P., Murray, N., Boccippio, D.J., 2007. Lightning charge retrievals: dimensional reduction, LDAR constraints, and a first comparison with LIS satellite data. J. Atmos. Ocean. Technol. 24, 1817–1838. https://doi.org/10.1175/ JTECH2089.1.
- Kostinskiy, A.Y., Syssoev, V.S., Bogatov, N.A., Mareev, E.A., Andreev, M.G., Makalsky, L. M., et al., 2015a. Observation of a new class of electric discharges within artificial clouds of charged water droplets and its implication for lightning initiation within thunderclouds. Geophys. Res. Lett. 42, 8165–8171. https://doi.org/10.1002/2015.GL065620.
- Kostinskiy, A.Y., Syssoev, V.S., Bogatov, N.A., Mareev, E.A., Andreev, M.G., Makalsky, L. M., et al., 2015b. Infrared images of bidirectional leaders produced by the cloud of charged water droplets. J. Geophys. Res. Atmos. 120, 10,728–10,735. https://doi.org/10.1002/2015JD023827.
- Kostinskiy, A.Y., Syssoev, V.S., Bogatov, N.A., Mareev, E.A., Andreev, M.G., Bulatov, M. U., Makal'sky, L.M., Sukharevsky, D.I., Rakov, V.A., 2016. Observations of the connection of positive and negative leaders in meter-scale electric discharges generated by clouds of negatively charged water droplets. J. Geophys. Res. Atmos. 121, 9756–9766. https://doi.org/10.1002/2016JD025079.
- Kostinskiy, A., Marshall, T., Stolzenburg, M., 2020. The mechanism of the origin and development of lightning from initiating event to initial breakdown pulses (v.2). J. Geophys. Res. Atmos. 125 https://doi.org/10.1029/2020JD033191.
- Lyu, F., Cummer, S.A., McTague, L., 2015. Insights into high peak current in-cloud lightning events during thunderstorms. Geophys. Res. Lett. 42, 6836–6843. https:// doi.org/10.1002/2015GL065047.

- Lyu, F., Cummer, S.A., Briggs, M., Marisaldi, M., Blakeslee, R.J., Bruning, E., et al., 2016. Ground detection of terrestrial gamma ray flashes from distant radio signals. Geophys. Res. Lett. 43, 8728–8734. https://doi.org/10.1002/2016GL070154.
- Marshall, T., Stolzenburg, M., Karunarathne, S., Cummer, S., Lu, G., Betz, H.-D., Briggs, M., Connaughton, V., Xiong, S., 2013. Initial breakdown pulses in intracloud lightning flashes and their relation to terrestrial gamma ray flashes. J. Geophys. Res. Atmos. 118, 10,907–10,925. https://doi.org/10.1002/jgrd.50866.
- Murphy, M.J., Cummins, K.L., Demetriades, N.W.S., Roeder, W.P., 2008. Performance of the new four-dimensional lightning surveillance system (4DLSS) at the Kennedy Space Center/Cape Canaveral Air Force Station complex. In: Paper presented at the 13th Conf on Aviation, Range, and Aerospace Meteorology. Paper 7.6, New Orleans, LA. 18 pp.
- Marshall, T., Karunarathne, S., Stolzenburg, M., Briggs, M., Cramer, E.S., Mailyan, B.G., McBreen, S., Roberts, O.J., Stanbro, M., 2017. Electric field change measurements of a terrestrial gamma ray flash. J. Geophys. Res. Atmos. 122, 5259–5266. https://doi.org/10.1002/2016JD026281.
- Mezentsev, A., Østgaard, N., Gjesteland, T., Albrechtsen, K., Lehtinen, N., Marisaldi, M., Smith, D., Cummer, S., 2016. Radio emissions from double RHESSI TGFs. J. Geophys. Res. Atmos. 121, 8006–8022. https://doi.org/10.1002/2016JD025111.
- Nag, A., Rakov, V.A., 2010a. Compact intracloud lightning discharges: 1. Mechanism of electromagnetic radiation and modeling. J. Geophys. Res. 115 https://doi.org/ 10.1029/2010JD014235. D20102.
- Nag, A., Rakov, V.A., 2010b. Compact intracloud lightning discharges: 2. Estimation of electrical parameters. J. Geophys. Res. 115 https://doi.org/10.1029/ 2010JD014237. D20103.
- Ogawa, T., Brook, M., 1964. The mechanism of the intracloud lightning discharge.

 J. Geophys. Res. 69 (24), 5141–5150. https://doi.org/10.1029/JZ069i024p05141.
- Rakov, V.A., Dulzon, A.A., 1987. Calculated electromagnetic fields of lightning return stroke. Tekhnisches Elektrodinamiks 1, 87–89
- Shao, X.M., Heavner, M., 2006. On the VLF/LF radiation pulse shapes at the initial milliseconds of lightning discharges. In: Proceeding of Electromagnetic Compatibility, 2006. EMC-Zurich 2006. 17th International Zurich Symposium on Singapore. IEEE Piscataway, N.I. pp. 402-404.
- Singapore. IEEE, Piscataway, NJ, pp. 402–404.
 Shao, X.M., Krehbiel, P.R., 1996. The spatial and temporal development of intracloud lightning. J. Geophys. Res. 101, 26641–26668.
- Shi, D., Wang, D., Wu, T., Takagi, N., 2019. Temporal and Spatial characteristics of preliminary breakdown pulses in intracloud lightning flashes. J. Geophys. Res. Atmos. 124, 12901–12914. https://doi.org/10.1029/2019JD031130.
- da Silva, C.L., Pasko, V.P., 2015. Physical mechanism of initial breakdown pulses and narrow bipolar events in lightning discharges. J. Geophys. Res. Atmos. 120, 4989–5009. https://doi.org/10.1002/2015JD023209.
- Smith, L.G., 1957. Intracloud lightning discharges. Q. J. R. Meteorol. Soc. 83, 103-111.
- Smith, E.M., Marshall, T.C., Karunarathne, S., Siedlecki, R., Stolzenburg, M., 2018. Initial breakdown pulse parameters in intracloud and cloud-to-ground lightning flashes.
 J. Geophys. Res. Atmos. 123, 2129–2140. https://doi.org/10.1002/2017JD027729.
- Stolzenburg, M., Marshall, T.C., Karunarathne, S., Karunarathna, N., Vickers, L.E., Warner, T.A., Orville, R.E., Betz, H.-D., 2013. Luminosity of initial breakdown in lightning. J. Geophys. Res. Atmos. 118 https://doi.org/10.1002/jgrd.50276.
- Stolzenburg, M., Marshall, T.C., Karunarathne, S., Karunarathna, N., Orville, R.E., 2014. Leader observations during the initial breakdown stage of a lightning flash. J. Geophys. Res. Atmos. 119, 12,198–12,221. https://doi.org/10.1002/2014JD021994.
- Stolzenburg, M., Marshall, T.C., Karunarathne, S., Orville, R.E., 2016. Luminosity with intracloud-type lightming initial breakdown pulses and terrestrial gamma-ray flash candidates. J. Geophys. Res. 121, 10,919–10,936. https://doi.org/10.1002/ 2016.JD025202.
- Stolzenburg, M., Marshall, T. C., & Karunarathne, S. (2020). On the transition from initial leader to stepped leader in negative cloud-to-ground lightning. Journal of Geophysical Research: Atmospheres, 125, e2019JD031765. https://doi.org/10.1029/2019JD031765.
- Stolzenburg, M., Marshall, T.C., Bandara, S., Hurley, B., Siedlecki, R., 2021. Ultra-high speed video observations of intracloud lightning flash initiation. Meteorol. Atmos. Phys. https://doi.org/10.1007/s00703-021-00803-3.
- Thomas, R.J., Krehbiel, P.R., Rison, W., Hunyady, S.J., Winn, W.P., Hamlin, T., Harlin, J., 2004. Accuracy of the lightning mapping array. J. Geophys. Res. 109, D14207 https://doi.org/10.1029/2004JD004549.
- Uman, M.A., McLain, D.K., Krider, E.P., 1975. The electromagnetic radiation from a finite antenna. Am. J. Phys. 43, 33–38.
- Villanueva, Y., Rakov, V.A., Uman, M.A., Brook, M., 1994. Microsecond-scale electric field pulses in cloud lightning discharges. J. Geophys. Res. 99, 14,353–14,360. https://doi.org/10.1029/94JD01121.
- Watson, S.S., Marshall, T.C., 2007. Current propagation model for a narrow bipolar pulse. Geophys. Res. Lett. 34, L04816 https://doi.org/10.1029/2006GL027426.
- Weidman, C.D., Krider, E.P., 1979. The radiation field waveforms produced by intracloud lightning discharge processes. J. Geophys. Res. 84 (C6), 3159–3164.
- Zhu, B., Zhou, H., Ma, M., Lv, F., Tao, S., 2010. Estimation of channel characteristics of narrow bipolar events based on the transmission-line model. J. Geophys. Res. 115, D19105 https://doi.org/10.1029/2009JD012021.